frontiers | Frontiers in Earth Science

TYPE Original Research
PUBLISHED 17 September 2025
DOI 10.3389/feart.2025.1657965

OPEN ACCESS

EDITED BY
Xiao-Ping Xia,
Chinese Academy of Sciences (CAS), China

REVIEWED BY
Liang Qiu,
China University of Geosciences, China
Hong-Peng Fan,
Chinese Academy of Sciences, China
Xiangsong Wang,
The University of Hong Kong, Hong Kong SAR, China

*CORRESPONDENCE
Wu Wei,
weiwu@sml-zhuhai.cn

RECEIVED 02 July 2025
ACCEPTED 18 August 2025
PUBLISHED 17 September 2025

CITATION
Wei W, Liu C-Z, Yan W and Zhong L-F (2025) Petrogenesis of andesites in a Triassic volcanic arc in the southern South China Sea: constraints from whole-rock and mineral geochemistry.
Front. Earth Sci. 13:1657965.
doi: 10.3389/feart.2025.1657965

Petrogenesis of andesites in a Triassic volcanic arc in the southern South China Sea: constraints from whole-rock and mineral geochemistry

Wu Wei[1]*, Chuan-Zhou Liu[2,3,4], Wen Yan[4,5] and Li-Feng Zhong[1]

[1]Southern Marine Science and Engineering Guangdong Laboratory (Zhuhai), Zhuhai, China, [2]State Key Laboratory of Lithospheric and Environmental Coevolution, Institute of Geology and Geophysics, Chinese Academy of Sciences, Beijing, China, [3]Laoshan Laboratory, Qingdao, China, [4]University of Chinese Academy of Sciences, Beijing, China, [5]Key Laboratory of Ocean and Marginal Sea Geology, South China Sea Institute of Oceanology, Innovation Academy of South China Sea Ecology and Environmental Engineering, Chinese Academy of Sciences, Guangzhou, China

Calc-alkaline andesitic rocks are prominently exposed as a major product of subduction-related magmatism. The identification of Late Triassic andesites in Meiji Atoll, located in the southern South China Sea (SCS), provides new insights into the regional magmatic evolution and geodynamic setting of the southern SCS margin during the early Mesozoic era. Here, we present structured illumination microscopy (SIMS) U-Pb zircon ages, zircon Hf-O isotopic compositions, whole-rock and mineral geochemistry, as well as Sr-Nd-Hf-Pb isotopic compositions of andesites drilled in the Meiji Atoll. Geochronological results indicate that the crystallization ages of the andesites range from approximately 217 Ma to 225 Ma, which coincide with the eruption of interbedded dacites. The Meiji calc-alkaline andesites are characterized by a strong fractionation between light rare earth elements (LREEs) and heavy rare earth elements (HREEs), an enrichment of large ion lithophile elements (LILEs) such as Rb, K, U, and Pb, and a depletion of high-field strength elements (HFSEs), particularly Nb, Ta, and Ti, when compared to normal mid-ocean ridge basalts (N-MORB). These characteristics align with the typical geochemical signature of average continental arc andesites. The andesites display relatively high initial $^{87}Sr/^{86}Sr$ ratios (0.7083–0.7113), slightly enriched $\varepsilon_{Nd}(t)$ values (–6.07 to –4.9) and $\varepsilon_{Hf}(t)$ values (–7.70 to –2.16), along with variable zircon $\varepsilon_{Hf}(t)$ and $\delta^{18}O$ values ranging from –2.93 to –1.99‰ and 4.0‰–9.0‰, respectively. The geochemical features of the andesites and zircons suggest they likely originated from a phlogopite-bearing metasomatized lithospheric mantle that had been influenced by subduction sediment compositions. Additionally, the geochemical characteristics and thermobarometry results of amphibole phenocrysts imply continuous and cryptic amphibole fractionation during the evolution of the arc magma. U-Pb ages and Hf isotopic data from the zircon xenocrysts exhibit a similar pattern to those from the eastern South China Block, providing compelling evidence for the existence of a Paleoproterozoic crystalline basement beneath the Nansha Block, akin to the Cathaysia Block. The identified volcanism at Meiji Atoll likely reflects the spatial variation in the distribution of arc magmatism along the South

China Block. It might also represent the earliest re-initiation of continental arc magmatism following a phase of flat-slab subduction of the paleo-Pacific.

KEYWORDS

South China Sea, zircon U-Pb geochronology, Calc-alkaline andesite, geochemistry, Arc magmatism, paleo-pacific subduction

1 Introduction

Calc-alkaline andesitic rocks are generally considered to be extensively distributed on active continental margins and island arcs. They represent an important constituent of the continental crust from the Precambrian to the present (Grove et al., 2012; Kelemen and Behn, 2016), which is consistent with the fact that continental crust has significant similarities in geochemical compositions to continental arc andesites (Taylor, 1967; Rudnick and Fountain, 1995). Therefore, the petrogenesis of calc-alkaline andesites has been a long-debated topic and is crucial for understanding the magmatic evolution of active margins (Taniuchi et al., 2020; Azizi et al., 2021).

Many hypotheses have been proposed to explain the genesis of andesitic magma, including 1) crystal differentiation from mantle-derived primary basaltic magma (Yoder and Tilley, 1962; Sisson and Grove, 1993; Lee and Bachmann, 2014) in combination with upper and lower crustal contamination (Annen et al., 2005); 2) partial melting of the basaltic rocks in the lower to middle crust (Smith and Leeman, 1987; Jackson et al., 2003); 3) partial melting of mantle peridotite under low-pressure or high-water concentration (Hirose, 1997; Tamura et al., 2016); 5) magma mixing/mingling between mafic and felsic magmas (Tatsumi et al., 2008; Kent et al., 2010). Large volumes of andesite and related magma at continental arc and island arc volcanoes are likely produced by melting, assimilation, storage, and homogenization (MASH)-like processes (Azizi et al., 2021). Source mixing relating to oceanic crust subduction, recycling of crustal components, melt–peridotite reaction, and involvement of slab-metasomatized mantle are also responsible for the generation of subduction zone andesitic melts (Anderson, 1976; Kelemen et al., 2007; Mitchell and Grove, 2015; Chen and Zhao, 2017; Chen et al., 2021). Fluid and melt originated from dehydration and dehydration melting of the subducting hydrated lithosphere composed of sediment, hydrothermally altered oceanic crust, and lithospheric mantle may play a key role in the formation of andesitic magma by melting within the mantle wedge in active margins (Miller and Christensen, 1994; Plank and Langmuir, 1998; Kelley et al., 2005; Behn et al., 2011). Partial melts from metasomatized peridotite and secondary pyroxenite lithologies that were generated by the reaction of slab-derived melts with the mantle wedge peridotite, then mixed in variable proportions to produce primary calc-alkaline andesites, were also recorded along the active margins, reflecting a particular mechanism of mantle processing in the subduction environment (Straub et al., 2008; Straub et al., 2011). Furthermore, partial melting and subsequent diapirism of subduction mélanges derived from physical mixing of slab components and the mantle wedge along the slab–mantle interface can form intermediate volcanoes without the intervention of parental basalts, implying that a significant proportion of the subducted continental crust is being reincorporated back into continents by primitive intermediate arc magmatism (Nielsen and Marschall, 2017; Gómez-Tuena et al., 2018). The processes involved in the assimilation of mélanges into the mantle wedge possess great potential to transfer the subduction signatures observed in natural arc magmas from the slab to the source of arc magmas (Codillo et al., 2018).

In this study, the Late Triassic calc-alkaline andesitic lavas drilled in the Meiji Atoll of the southern South China Sea (SCS) region may provide new constraints on the factors that control the genesis of calc-alkaline magmatism. We carried out comprehensive analyses of SIMS U-Pb zircon ages, Hf-O isotopic compositions, whole-rock and mineral geochemistry, and Sr-Nd-Hf-Pb isotopic compositions for Late Triassic Meiji Atoll calc-alkaline andesites, in an attempt to 1) determine the eruption time for the andesitic magma, 2) decipher and constrain the petrogenetic processes, and 3) deepen our understanding of the regional magmatic evolution and geodynamic setting and evaluate the influence of early Mesozoic paleo-Pacific subduction.

2 Geological settings and sample description

2.1 Geological setting

The South China Sea (SCS), located to the south of the South China Block (SCB), is composed of the northern continental margin, a deep-water basin, and the southern continental margin (Yan et al., 2010). Currently, the SCS, interpreted as a plate-edge basin, is surrounded by four distinct tectonic zones, including a subduction zone in the east, a strike–slip fault zone in the west, a collisional thrust belt in the south, and a rifted passive margin in the north (Li et al., 2021). The deep-water basin of the SCS can be further divided into three sub-basins, including the East sub-basin, the Southwest sub-basin, and the Northwest sub-basin (Figure 1). The extensively thinned continental crust varies from ~6 km to ~30 km thick around the deep-water basin (Hayes and Nissen, 2005). Unlike open oceans and other small back-arc basins in the West Pacific, the SCS deposited thick terrigenous sediments on the continental shelf without large abyssal fans (Huang and Wang, 2006). The northern continental margin of the SCS is characterized by the widely distributed (over 250 km) detachment faults, widespread high-velocity lower crust (HVLC) and magmatic intrusion below thinned crust, a large number of landward dipping fault systems, and the fast transition from continental margin to seafloor spreading (Sun et al., 2019).

Recent U-Pb age determinations for borehole-penetrated plutonic rocks imply a Late Jurassic amphibole plagiogneiss

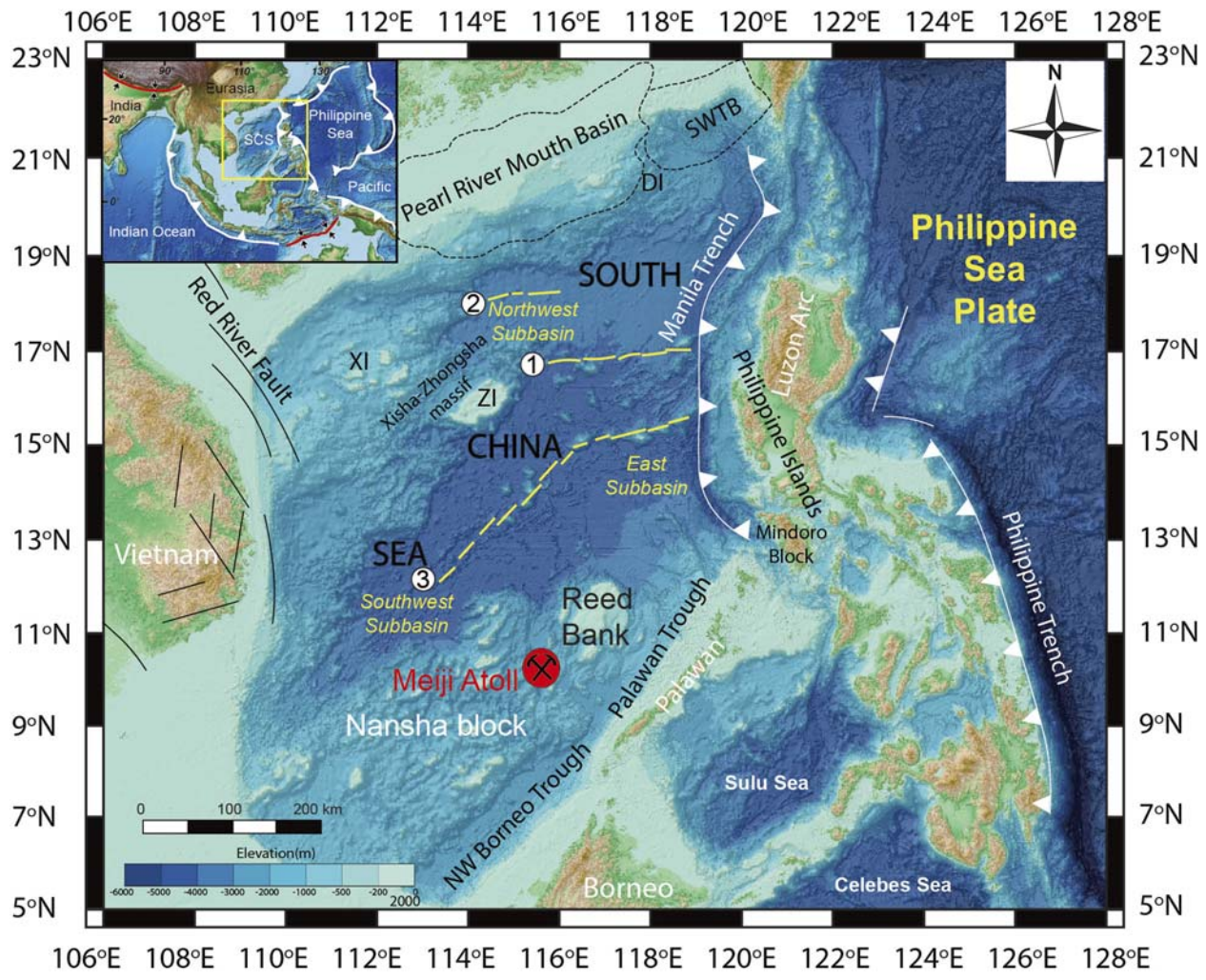

FIGURE 1
Tectonic sketch map of the area around the South China Sea. BBWB = Beibuwan basin; SWTB = Southwest Taiwan basin. White circles 1, 2, and 3 represent the fossil spreading mid-ocean ridges with ages of ~33–23.6 Ma, ~30–28.5 Ma, and ~23.6–15 Ma, respectively. The black solid line represents the lithospheric faults, and the white solid line with white triangles represents the subduction zone.

basement for the northern continental margin of the SCS, which was later intruded by Early Cretaceous plutons (Zhu et al., 2017). Previously sampled rocks indicate that the southern margin of the SCS, including the Nansha Block and the Reed Bank-Northeastern Palawan Block area, was once a part of the South China continent (Kudrass et al., 1986; Yan et al., 2010; Miao et al., 2021). Since the Mesozoic, the realm of the SCS has experienced the subduction of the paleo-Pacific (Taylor and Hayes, 1983). After a Cretaceous to Paleogene period of extension and rifting, which affected tectonic deformation in the upper crust (Savva et al., 2014) and the rheological properties of the lower crust (Ros et al., 2017) and resulted in the formation of numerous NE–SW-trending half-grabens (Tang et al., 2014), the continental fragments, including the Nansha, Reed Bank, Palawan, and Mindoro Blocks, were finally separated from the South China continent and drifted southward to their current position as the transition from plate subduction to seafloor spreading occurred during the Cenozoic (Kudrass et al., 1986).

2.2 Sample description

The borehole NK-1 drilled on the Meiji Atoll of the southern SCS continental margin penetrated the volcanic basement that consists of volumes of dacitic, interbedded with basaltic and andesitic rocks from 1010 to 2020 mbsf (meters below sea floor). The studied andesitic rocks were interbedded with the dacites and basalts. The depth of the andesitic rocks collected from the borehole NK-1 is 1319.06–1446.09 mbsf, and the thickness of the andesitic rocks ranges from 0.05 m to 0.2 m. The andesitic rocks are dark gray in color with massive structures, commonly with porphyritic texture consisting of subhedral phenocrysts or microphenocrysts including plagioclases and pale green-brown amphiboles (Figure 2). These andesites also show calcite, sericite, chlorite, epidote, and iron oxides as secondary phases. The groundmass is characterized by randomly distributed acicular plagioclase laths and amphibole crystallites embedded in cryptocrystalline materials.

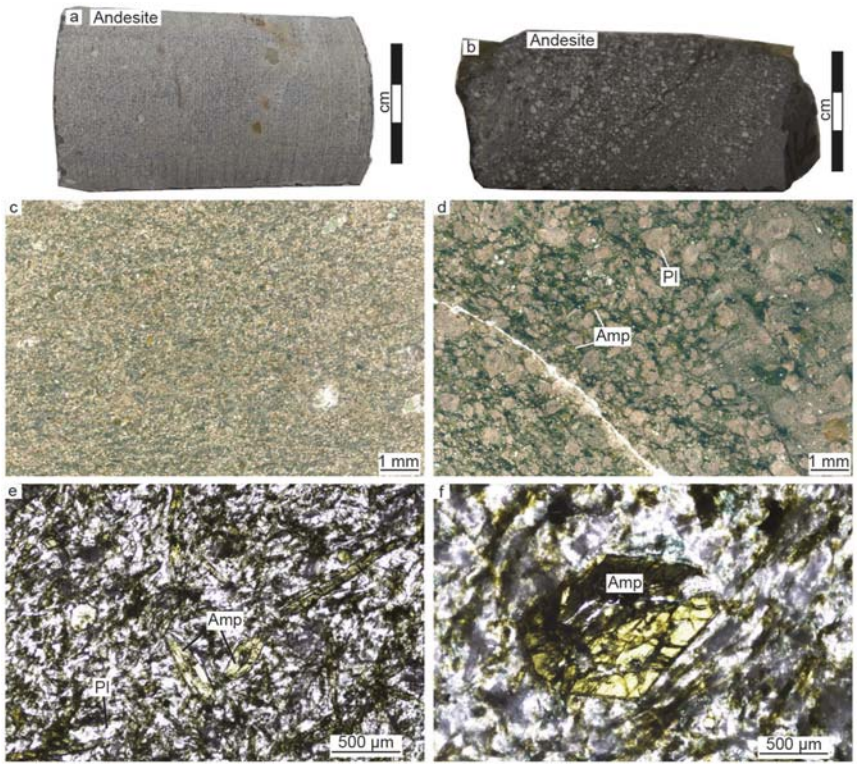

FIGURE 2
Representative hand-specimen and photomicrographs for the andesitic rocks from the Meiji Atoll, southern South China Sea: **(a,b)** Andesite hand-specimen with phenocrysts of plagioclase and amphibole; **(c,d)** Thin section photomicrographs of sericite-altered plagioclase and chlorite-altered amphibole phenocrysts with different sizes; **(d)** Amphibole phenocrysts are variably acicular to fibrous in habit; **(e,f)** Amphibole phenocrysts are idiomorphic in habit; Abbreviations: Pl, plagioclase; Amp, amphibole.

3 Analytical techniques

The U-Pb dating and Hf-O isotopes of the zircons from andesites, bulk-rock and mineral major and trace elements, and Sr-Nd-Hf-Pb isotopes of the andesites were all carried out in the Institute of Geology and Geophysics, Chinese Academy of Sciences (IGGCAS), in Beijing, China. Analytical results are presented in the Supplementary Tables S1–S7.

3.1 Zircon U-Pb ages and Hf-O isotopes of the andesites

Zircons were separated from four andesite samples, using conventional hydroseparation and magnetic methods, followed by handpicking under a binocular microscope. The zircon grains were mounted in an epoxy resin disk, polished, and coated with gold. These grains were examined and imaged before analysis using a transmitted and reflected optical microscope and cathodoluminescence to determine crystal shapes and internal structures and to pick positions for spot analyses. Zircon U-Pb dating was undertaken by a CAMECA IMS-1280HR ion microprobe. The analytical procedures for zircon U-Pb geochronology were similar to those of Li X.-H. et al. (2009). Uncertainties of isotope ratios were at the 1σ level, and the calculated ages are reported for 2σ confidence. Data reduction was carried out using Isoplot 3.0 (Ludwig, 2000). The Qinghu zircon standard was used as an unknown sample to check the stability and accuracy of the measurement process. The operating condition was described by Li X. et al. (2009). Oxygen isotopes were examined using the CAMECA IMS-1280 ion microprobe, following the description of Li X.-H. et al. (2009) and Li et al. (2010). After U-Pb dating and O isotopic analysis of zircons, *in situ* zircon Lu-Hf isotope analyses were performed using a Neptune MC-ICP-MS equipped with a 193-nm laser ablation system. The detailed analytical procedure and correction for interference are similar to those of Wu et al. (2006). The obtained weighted mean $^{176}Hf/^{177}Hf$ ratios of the zircon standard Mud Tank and SA01 agree with the recommended values (Woodhead and Hergt, 2007).

3.2 Whole-rock major and trace elements

The altered or weathered portion of the andesites was excised, and the remaining parts of the blocks were cut into small pieces. Half of these pieces were polished into thin sections, and the remaining rock chips were crushed and then powdered to a grain size of 200 mesh in an agate mill for bulk-rock analyses. Bulk-rock major element compositions were determined by the AXIOS Minerals X-ray fluorescence (XRF) spectrometry on

fused lithium-tetraborate glass beads. The analytical precision for major elements ranges from 1% to 3%. Bulk-rock trace elements (including rare earth elements) were analyzed by an Agilent 7500a inductively coupled plasma mass spectrometry (ICP-MS), following the description of Yang J. H. et al. (2012). The powdered samples (approximately 50 mg) were dissolved in high-pressure Teflon vessels using a highly purified HF + HNO_3 mixture for 5 days at 150 °C. Rhodium (Rh) was added as an internal standard to monitor signal drift during analysis. Standard materials BIR-1a, RGM-2, GSR-3, and BHVO-2, which were analyzed along with samples, were used for analytical quality control, indicating the analytical errors were better than 5%.

3.3 Major and trace element analysis for mineral

Major element compositions of amphibole from andesites using a JEOL JXA-8100 electron probe microanalyzer (EPMA) operated in wavelength-dispersive spectrometer (WDS) mode. Operating conditions included an accelerating voltage of 15 kV, a beam current of 20 nA, a beam size of 5 μm, and counting times of 20–60 s. Energy-dispersive spectrometry (EDS) in combination with backscattered electron scanning (BSE) imaging was used to select spot locations for quantitative *in situ* analysis. The amphiboles were analyzed for Na, Cr, Mg, Si, Mn, K, Al, Ti, Fe, Ca, F, Cl, and Ni. The standard minerals and synthetic oxides used in these analyses for calibration included albite (Na), chromium oxide (Cr), olivine (Mg), bustamite (Mn), K-feldspar (K), jadeite (Al), rutile (Ti), magnetite (Fe), riebeckite (F), tugtupite (Cl), and diopside (Ca and Si). Atomic number-absorption-fluorescence (ZAF) correction routines were used to process the raw analytical results. The accuracy was better than 1%–5% for major elements (≥1wt%), and that of the minor element (<1 wt%) analyses was better than 10%. The precision was better than 1 wt% for element oxides. The analytical results of major and minor elements for amphibole are presented in Supplementary Table S6.

In situ trace element contents of amphibole and zircon were determined by laser ablation-inductively coupled plasma mass spectrometry (LA-ICP-MS) employing an Agilent 7500a Q-ICP-MS instrument (Agilent Technologies, United States) coupled to a 193 nm ArF excimer laser system (Geolas HD, Lambda Physik, Göttingen, Germany). The approach is similar to those outlined in Xie et al. (2008) and Wu et al. (2018), with isotopes measured using a peak-hopping mode with a laser beam diameter of ca. 60 μm and a 6 Hz repetition rate. The laser energy density is ~4.0 J/cm^2. Helium gas was employed as the carrier gas to improve the transportation efficiency of ablated aerosols, and nitrogen gas was used as an additional gas to enhance sensitivity. Before analyzing the amphibole and zircon, the LA-ICP-MS system was optimized using NIST SRM 610 reference glass as the calibration material to achieve the maximum signal intensity and low oxide rates. Glass reference materials ARM-1 (Wu et al., 2019) and BCR-2G were also analyzed for data quality control. Multiple or single LA analyses for Amp were undertaken in conjunction with single-electron microprobe analyses during the experiment. Silicium (^{29}Si) content values previously obtained by electron probe microanalysis were used as an internal standard to quantify elemental concentrations of amphibole and zircon. Off-line selection and integration of background and analyte signals, time-drift corrections, and quantitative calibrations were performed using the GLITTER program (Griffin et al., 2008) for data reduction. The measured values of reference materials were in agreement with the recommended values. For most trace elements (>0.10 μg/g), the accuracy is better than ±10% with analytical precision (1 RSD) of ±10%. The analytical results of trace element compositions for amphibole and zircon are presented in Supplementary Table S5, S7, respectively.

3.4 Whole-rock Sr-Nd-Hf-Pb isotopes

Measurements of the Sr-Nd-Hf isotopic ratios were performed using a Neptune Plus multi-collector inductively coupled plasma mass spectrometer following the description of Yang et al. (2010). The powdered samples (about 100 mg) were dissolved in high-pressure Teflon vessels using a highly purified, concentrated HF + HNO_3+$HClO_4$ (2 mL+1 mL + 0.2 mL) mixture for 7 days at 150 °C. The solutions were then evaporated to fume $HClO_4$. A 1-mL aliquot of 6 M HCl was added to the Teflon vessel and dried, and then this procedure was repeated once. After it cooled, 5 mL of 3 M HCl was added to the residue. The Teflon vessel was placed on a hot plate at 100 °C for 12 h, and then the sample solution was loaded onto pre-conditioned 2 mL Ln Spec resin.

Light and middle rare earth elements (LMREE) were eluted first, and then the Lu (+Yb) fraction was eluted. After separating the Ti from Hf, Hf (+Zr) was extracted from the column with HF. Then, the solution of Hf (+Zr) was evaporated to dryness, and 1 mL of 2% HNO3 was added to the residue. The solution was ready for Hf analysis. The solution of LMREE was dried and re-dissolved in 1.5 mL of 2.5 M HCl. After loading the solution into a quartz column packed with AG50W-X12, Rb and Sr were eluted. Then, the LMREE fraction was stripped out with 6 mL of 6 M HCl. After the LMREE collections were dried and re-dissolved in 0.5 mL of 0.25 M HCl, the solutions were loaded onto Ln Spec resin. Then, the Nd and Sm were eluted by an appropriate amount of acid.

The measured ^{87}Sr/^{86}Sr, ^{143}Nd/^{144}Nd and ^{176}Hf/^{177}Hf ratios were corrected for mass fractionation using ^{87}Sr/^{86}Sr = 0.1194, ^{143}Nd/^{144}Nd = 0.7219, and ^{176}Hf/^{177}Hf = 0.7325, respectively. During the analytical sessions, the measured values for the NBS987 Sr standard, the JNdi-1 Nd standard, and the Alfa Hf standard were 0.710277 ± 24 (2σ, n = 10) for ^{87}Sr/^{86}Sr, 0.512107 ± 10 (2σ, n = 10) for ^{143}Nd/^{144}Nd, and 0.282192 ± 14 (2σ, n = 12) for ^{176}Hf/^{177}Hf, respectively. BHVO-2 and BIR-1 were measured along with the samples and gave rise to the ^{87}Sr/^{86}Sr, ^{143}Nd/^{144}Nd, and ^{176}Hf/^{177}Hf ratios of 0.703481 ± 12 and 0.703101 ± 11, 0.512987 ± 12 and 0.513124 ± 13, and 0.283087 ± 10 and 0.283247 ± 20, respectively, which are in accordance with the reference values (GeoREM, http://georem.mpch-mainz.gwdg.de/). The total procedure blanks for the Sr isotope, Nd isotope, and Hf isotope were 240 pg, 70 pg, and 50 pg, respectively.

Measurement of the Pb isotopic ratio was performed using a Thermofisher Triton Plus multi-collector thermal ionization mass spectrometer following the description of Li et al. (2015). The powdered samples (approximately 100–120 mg) were completely dissolved in a Savillex Teflon screw-cap beaker using a highly

purified concentrate HF + HNO_3 mixture for 7 days at 160 °C. The Pb fraction with high purity was separated from the rock matrix using a HBr-HCl elution procedure on Teflon columns containing ~0.15 mL anion resin (AG1-X8, 100–200 mesh). The whole chemical procedural blank of Pb was approximately 200 pg. The Pb fraction with high purity was re-dissolved using a mixture solution of silica gel and H_3PO_4 and loaded onto a single-Re filament. International standard NIST 981 was used to monitor instrument stability during the period of data collection and correct mass fractionation. Measured Pb isotopic ratios were corrected for instrumental mass fractionation of 1.2‰ per atomic mass unit by reference to repeated analyses of the NIST 981 Pb standard.

4 Results

4.1 Geochronology

The elected zircons extracted from four andesite samples are mostly euhedral to subhedral in morphology, transparent, and light brown in color. Cathodoluminescence (CL) images show numerous blurry concentric zoning with low to variable luminescence (Figure 3), with variable Th (5.0–784 ppm), U (22.0–930 ppm), and higher Th/U ratios (0.24–1.95) than metamorphic-derived zircons (<0.1), revealing a magmatic origin. Some zircons from the sample NK-1-V2-91 show inherited cores with growth rims, implying the occurrence of inherited zircon crystals. The size of the zircons is from 40 μm to 100 μm in width, with the length to width ratios from 3:2 to 3:1. Four of 12 zircon grains from the sample NK-1-V2-91 yield concordant $^{206}Pb/^{238}U$ ages of 221.7 ± 3.6 Ma (MSWD = 0.12, n = 4) with a weighted mean age of 221.5 ± 7.9 Ma (MSWD = 0.39, n = 4), which represent the crystallization age of andesitic magma. The remaining eight ancient zircons, with $^{207}Pb/^{206}Pb$ ages between 1898 and 2467 Ma, represent the crystallization ages of inherited zircons entrained by the andesitic magma.

All 24 U-Pb analyses for NK-1-V2-139 yield $^{206}Pb/^{238}U$ ages between 207 Ma and 227 Ma with a weighted mean age of 217.7 ± 2.1 Ma (MSWD = 1.8, n = 24), representing the crystallization age of NK-1-V2-91. Zircons from NK-1-V2-166 yield a lower intercepted age of 222.8 ± 2.4 Ma, which is identical to their weighted average ^{207}Pb-corrected $^{206}Pb/^{238}U$ ages within uncertainties, that is, 223.1 ± 2.0 Ma. Zircons from NK-1-V2-171 yield concordant $^{206}Pb/^{238}U$ ages of 225.6 ± 3.0 Ma (MSWD = 0.38, n = 12) with a weighted mean age of 225.7 ± 3.8 Ma (MSWD = 2.8, n = 12), interpreted as the crystallization age of the sample (Figure 4).

4.2 Whole-rock geochemistry and Sr-Nd-Hf-Pb isotopic compositions

The whole-rock geochemistry results for four andesites from the Meiji Atoll are listed in Supplementary Table S2. In the plots of SiO_2 *versus* Nb/Y diagram (Winchester and Floyd, 1977) (Figure 5a), the andesitic rocks plot predominantly within the field of andesite. In the plots of Th *versus* Co diagram (Hastie et al., 2007) (Figure 5b), the andesites predominantly fall in the fields of high-K calc-alkaline and/or shoshonite series. After normalizing all major element compositions to 100% anhydrous, major element data on the andesites show limited variation in SiO_2 content (57.8–61.7 wt%), Al_2O_3 content (14.8–18.7 wt%), CaO content (3.61–7.48 wt%), MgO content (1.37–2.91 wt%), TFe_2O_3 content (7.40–9.48 wt%), TiO_2 contents (0.71–1.68 wt%), and LOI (loss on ignition) content (0.80–1.89 wt%). The content of total alkali (Na_2O+ K_2O) ranges from 3.82 wt% to 9.83 wt%, and the $Mg^{\#}$ also shows a wide variation with 28.57–43.19 (Figure 6a). Furthermore, most of the major elements for andesites show relatively linear trends on Harker diagrams (Figures 6b-d), such as Al_2O_3 (Figure 6b).

Samples have ΣREE concentrations ranging from 74 ppm to 386 ppm, with Ni ranging from 2.32 ppm to 9.10 ppm, Cr ranging from 18.4 ppm to 64.7 ppm, and Co ranging from 9.11 ppm to 23.8 ppm for the transitional trace element compositions. Four andesites show subparallel trace element patterns resembling those of average continental arc andesites on the chondrite-normalized rare earth element (REE) patterns (Figure 7a). On the primitive mantle-normalized trace element diagrams (Figure 7b), they are characterized by variable enrichment in light rare earth elements (LREEs) and large ion lithophile elements (LILEs, e.g., Rb, K, U, and Pb) and depletion of high-field strength elements (HFSEs, particularly Nb, Ta, and Ti) compared to normal mid-ocean ridge basalts (N-MORB), with $(La/Yb)_N$ ratios of 4.9–8.6. Weak negative Eu anomalies are observed in the andesitic samples ($Eu/Eu^* = 0.6–0.9$).

Whole-rock Sr-Nd-Hf-Pb isotopic data of the andesites are listed in Supplementary Table S2. The initial $^{87}Sr/^{86}Sr$, $^{206}Pb/^{204}Pb$, $^{207}Pb/^{204}Pb$, $^{208}Pb/^{204}Pb$ ratios and $\varepsilon_{Nd}(t)$ and $\varepsilon_{Hf}(t)$ values were recalculated based on the corresponding zircon U-Pb ages. The andesites have relatively high initial $^{87}Sr/^{86}Sr$ ratios (0.7083–0.7113) and display relatively limited variation in $\varepsilon_{Nd}(t)$ values of −6.07 to −4.91 and $\varepsilon_{Hf}(t)$ values of −7.70 to −2.16, with old Nd (1477–1675 Ma) and Hf (1172–1918 Ma) model ages. On the plot of $\varepsilon_{Hf}(t)$ *versus* $\varepsilon_{Nd}(t)$ isotopic diagram (Figure 8a), these samples define a subparallel linear trend resembling the Terrestrial Array ($\varepsilon_{Hf}(t) = 1.33 \times \varepsilon_{Nd}(t) + 3.19$ (Vervoort et al., 2011)), without significant Nd-Hf isotopic decoupling. The initial $^{206}Pb/^{204}Pb$, $^{207}Pb/^{204}Pb$, and $^{208}Pb/^{204}Pb$ ratios of the calc-alkaline andesites are generally higher than those of interbedded and intercalated basaltic rocks but lower than the volumes of dacites drilled from Meiji Atoll. All samples define the positive correlations in $(^{207}Pb/^{204}Pb)_i$ vs. $(^{206}Pb/^{204}Pb)_i$ and $(^{208}Pb/^{204}Pb)_i$ vs. $(^{206}Pb/^{204}Pb)_i$ diagrams (Figures 8c,d), subparallel to the Northern Hemisphere Reference Line (NHRL). In the plot of $(^{207}Pb/^{204}Pb)_i$ vs. $(^{206}Pb/^{204}Pb)_i$ diagram (Figure 8c), the andesites plot significantly above the NHRL and to the right side of the 4.55 Ga geochron line. They also show similar $(^{206}Pb/^{204}Pb)_i$, $(^{207}Pb/^{204}Pb)_i$, and $(^{208}Pb/^{204}Pb)_i$ ratios to the enriched mantle 2 (EM–II;) components, Middle to Late Jurassic basaltic rocks, and crust-derived suites in the Cathaysia Block.

4.3 Amphibole major and trace element compositions

The amphibole phenocrysts within the host andesites have been selected for *in situ* microprobe and laser ablation studies. Major and trace elements of amphiboles are listed

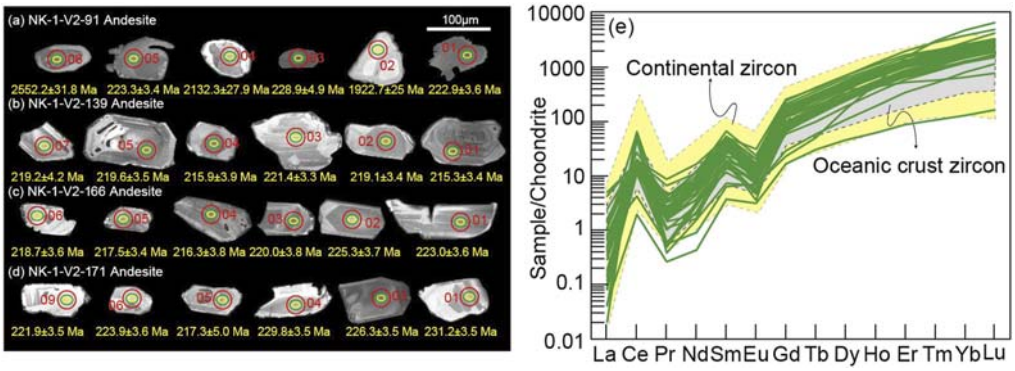

FIGURE 3
Cathodoluminescence images of representative zircons analyzed for U-Pb ages, Lu-Hf, and O isotopes **(a–d)**. Small ellipses indicate the SIMS analytical spots for U-Pb and O isotopes, and the large circles denote the LA-MC-ICP-MS analytical spots for Lu-Hf isotopes. SIMS spots are 30 microns in length for scale. Rare earth elements (REE) patterns of zircon grains determined by *in situ* analysis (LA-ICP-MS) for the Meiji andesites **(e)**. The values of continental and ocean crust zircons are from Grimes et al. (2007), and the normalized values for chondrite are from Sun and McDonough (1989).

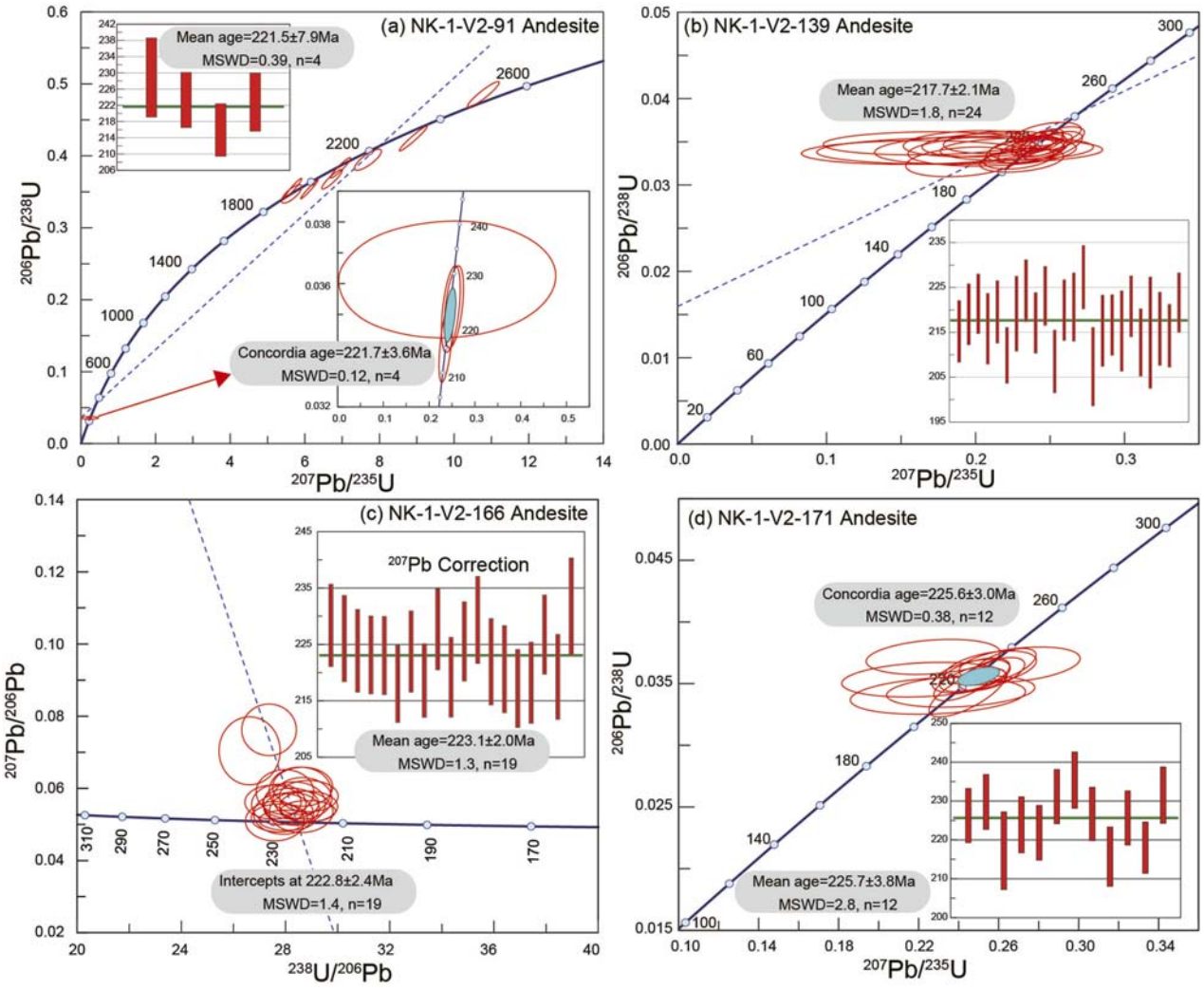

FIGURE 4
SIMS zircon U-Pb concordia diagram **(a,b,d)** and Terra–Wasserburg plots **(c)** for andesites from Meiji Atoll, southern South China Sea.

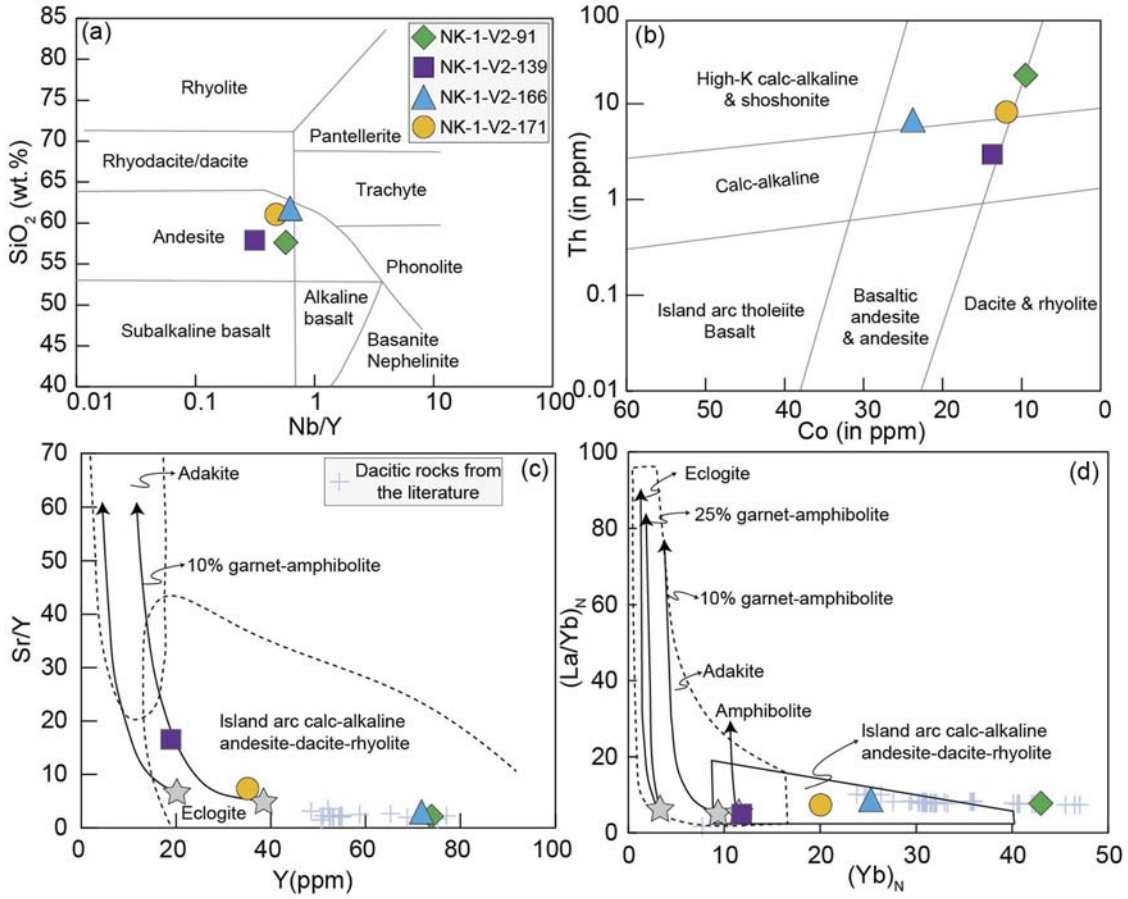

FIGURE 5
(a) Nb/Y vs. SiO_2 (after Winchester and Floyd, 1976), **(b)** Co vs.Th diagram (after Hastie et al., 2007), **(c)** $(La/Yb)_N$ vs. $(Yb)_N$ (after Defant and Drummond, 1990), and **(d)** Sr/Y vs. Y diagrams for Meiji andesites. Dacitic rocks from Wei et al. (2021).

in Supplementary Tables S6, S7, respectively. According to the nomenclature of Leake et al. (1997), the amphiboles from the Meiji andesites are mainly magnesio-hornblende, pargasite ($^{VI}Al > Fe^{3+}$), and magnesio-hastingsite ($^{VI}Al < Fe^{3+}$), with slight variations to actinolite, ferro-hornblende, and ferro-edenite (Figures 9a,b). These amphiboles are characterized by highly variable $Mg^{\#}$ values ranging from 0.34 to 0.78 for NK-1-V2-91, 0.48 to 0.83 for NK-1-V2-139, 0.65 to 0.96 for NK-1-V2-166, and 0.59 to 0.84 for NK-1-V2-171. The silica content ranges from 5.89 a.p.f.u to 7.55 a.p.f.u for NK-1-V2-91, 5.87 a.p.f.u to 7.56 a.p.f.u for NK-1-V2-139, 5.79 a.p.f.u to 7.52 a.p.f.u for NK-1-V2-166, and 5.86 a.p.f.u to 7.47 a.p.f.u for NK-1-V2-171. The alkali content (Na + K) is up to 0.70 a.p.f.u, and the Ti content is as high as 0.53 a.p.f.u. They show large variations in Cr (4.28–1290 ppm) and Ni (0.52–20.3 ppm) concentrations. The chondrite-normalized pattern of REE (Figures 7c-j) in amphibole phenocrysts is slightly convex upward with variable enrichment in middle-REEs (MREEs) relative to LREEs and HREEs (La_N/Sm_N = 0.16–0.83 and Gd_N/Yb_N = 0.85–2.04). Slightly to significantly negative Eu anomalies (Eu/Eu^*= 0.45–1.01) are also observed in these amphibole grains. The incompatible trace element diagram reveals variable depletion in Th, U, and P and enrichment in Rb, Ba, and K relative to the neighboring immobile elements (Figure 7).

4.4 Zircon trace elements, Lu-Hf, and O isotopic compositions

The trace element compositions of dating zircon grains were applied to monitor the geochemical signatures of their host magmas and elucidate the tectonic setting of drilled andesites (Supplementary Table S5). Chondrite-normalized rare earth element (REE) patterns for most of the analyzed zircon grains display significant positive Ce anomalies and negative Eu anomalies (Figure 3e), consistent with their magmatic origin. They are also characterized by the enrichment of HREEs and depletion of LREEs. The Yb and Hf contents of the analyzed zircons show relatively wide ranges of 13.78–851 ppm and 164–13,228 ppm, respectively. Nb and Y concentrations are also variable, with ranges of 0.88–9.0 ppm and 99.4–2033 ppm, respectively.

The results of *in situ* zircon Lu-Hf and O isotopic compositions from four andesite samples are listed in Supplementary Table S3. For the sample NK-1-V2-91, the initial $^{176}Hf/^{177}Hf$ ratios of Late Triassic zircons vary from 0.282555 to 0.282578, and the calculated $\varepsilon_{Hf}(t)$ values range from −2.93 to −1.99 (Figure 8e), with a $T_{DM1}(Hf)$ from 954 Ma to 979 Ma and $T_{DM2}(Hf)$ from 1377 Ma to 1433 Ma. Meanwhile, the initial $^{176}Hf/^{177}Hf$ ratios

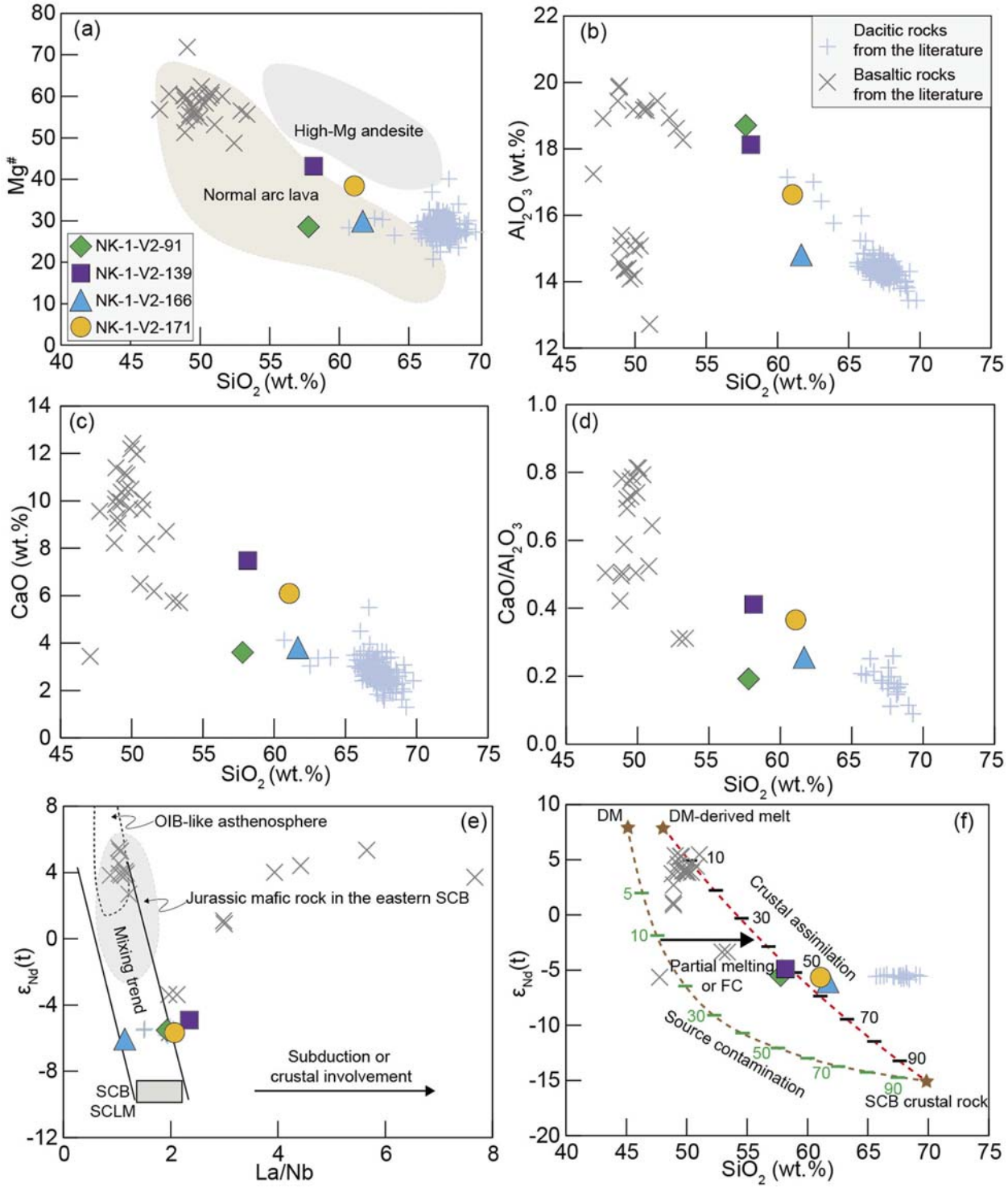

FIGURE 6
(a) $Mg^{\#}$ vs. SiO_2. The fields of normal arc lava and high-Mg andesite are from Gan et al. (2020). **(b)** Al_2O_3 vs. SiO_2. **(c)** CaO vs. SiO_2. **(d)** CaO/Al_2O_3 vs. SiO_2. **(e)** $\varepsilon_{Nd}(t)$ vs. La/Nb (after Gan et al., 2020 and references therein). **(f)** $\varepsilon_{Nd}(t)$ vs. SiO_2. The DM (depleted mantle) is marked by SiO_2 = 45 wt%, Nd = 4.0 ppm, $\varepsilon_{Nd}(t)$ = +8.0, and Nb/La = 0.75, its derivation is marked by SiO_2 = 48 wt%, Nd = 20 ppm, $\varepsilon_{Nd}(t)$ = +8.0, and Nb/La = 0.75, and the SCB crustal rock is marked by SiO_2 = 70 wt%, Nd = 26.3 ppm, εNd(t) = −15.0 (Gan et al., 2020). Basaltic rocks from Wei et al. (2021).

of the remaining eight inherited zircons from NK-1-V2-91 vary from 0.281308 to 0.281446, and the calculated $\varepsilon_{Hf}(t)$ values range from −6.26 to 2.85, with a $T_{DM1}(Hf)$ from 2499 Ma to 2699 Ma and $T_{DM2}(Hf)$ from 2641 Ma to 3060 Ma. For the samples NK-1-V2-139, 166, and 171, the initial $^{176}Hf/^{177}Hf$ ratios vary from 0.282197 to 0.282680, and the calculated $\varepsilon_{Hf}(t)$ values range from

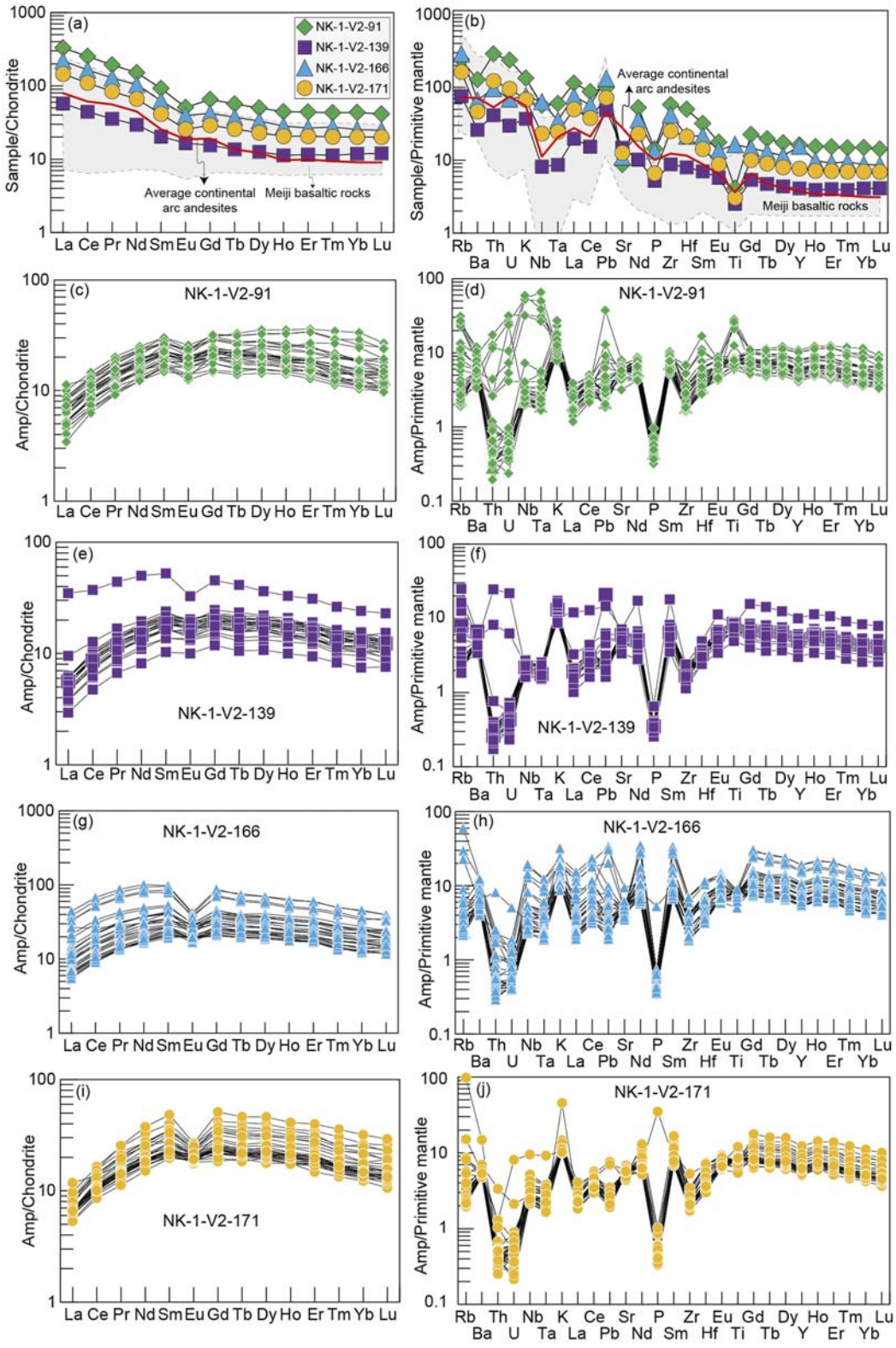

FIGURE 7
Chondrite-normalized REE patterns and primitive mantle-normalized trace element diagrams **(a,b)** represent andesites; **(c–j)** represent the amphibole phenocrysts for the Meiji dacites. Data source: Normalized values for chondrite and primitive mantle are from Sun and McDonough (1989). Average continental arc andesites are from Kelemen et al. (2003), and Meiji basaltic rocks are from Wei et al. (2021).

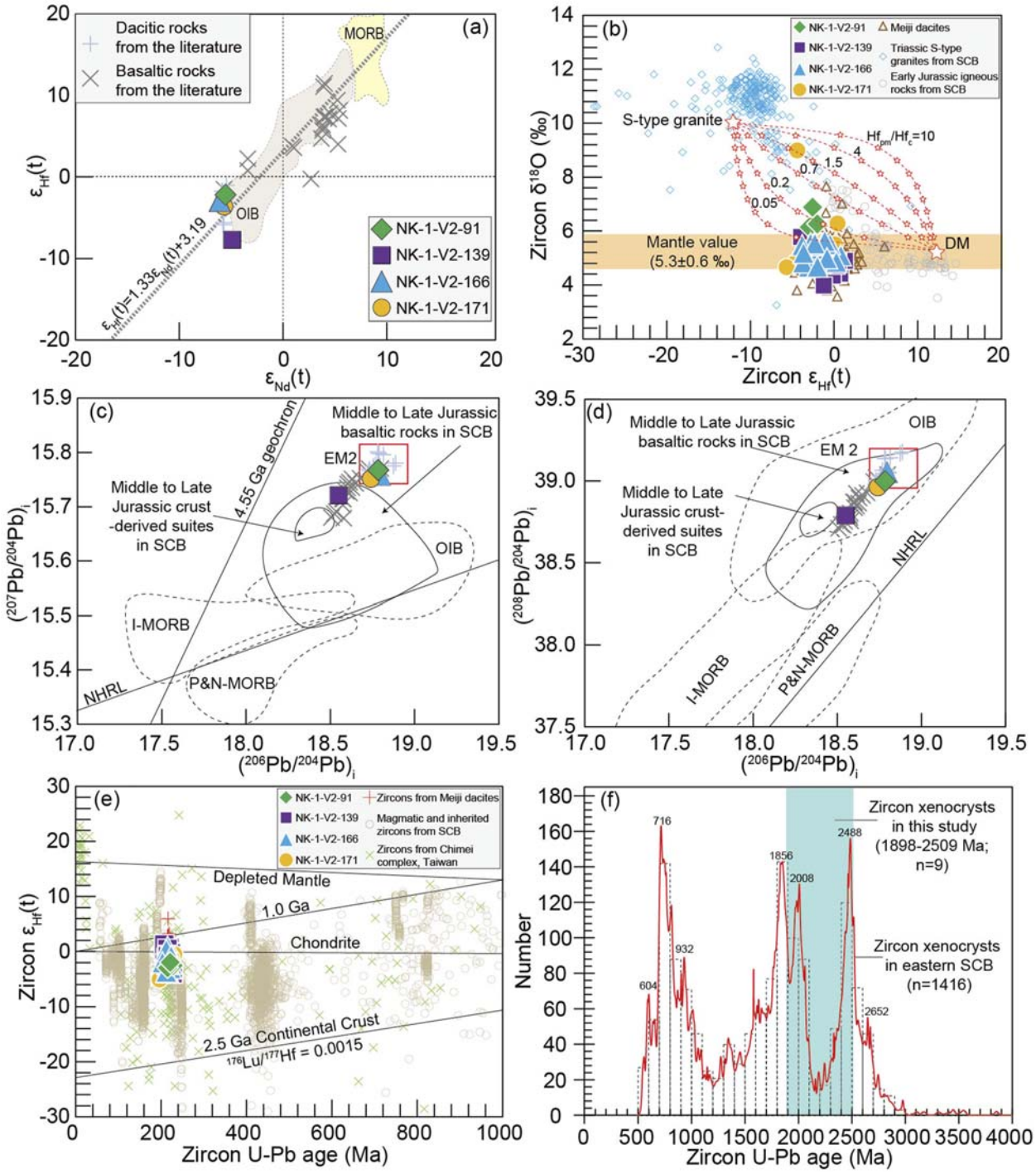

FIGURE 8
(a) $\varepsilon_{Nd}(t)$ vs. $\varepsilon_{Hf}(t)$ (after Feng et al., 2020 and references therein) diagram for the andesites; **(b)** Zircon Hf-O isotopic compositions for the andesites. Zircons from Meiji dacites (Wei et al., 2021), Triassic S-type granites (Jiao et al., 2015), and Early Jurassic igneous rocks (Yang et al., 2020) of the South China Block are plotted for comparison. The dotted lines are two-component mixing trends between depleted mantle- and S-type granite-derived magmas. Hf_{pm}/Hf_c is the ratio of the Hf content of the depleted mantle-derived magma (pm) over that of the crustal melt **(c)**, and the open pentagrams are at 10% mixing increments, assuming mantle zircon has an ε_{Hf} value of +12 and a $\delta^{18}O$ value of 5.3‰, and S-type granite zircon has an ε_{Hf} value of −12 and a $\delta^{18}O$ value of 10‰. **(c,d)** $(^{207}Pb/^{204}Pb)_i$ vs. $(^{206}Pb/^{204}Pb)_i$ and $(^{208}Pb/^{204}Pb)_i$ vs. $(^{206}Pb/^{204}Pb)_i$ diagrams for the andesites. Data sources: Middle-Late Jurassic basaltic rocks in the Cathaysia Block (Xie et al., 2006; Wang et al., 2008); Middle–Late Jurassic crust-derived suites in the Cathaysia Block (Li et al., 2013); I-MORB (Indian MORB), P&N-MORB (Pacific and Atlantic MORB), OIB, NHRL, and 4.55 Ga geochron (Hart, 1984; Barry and Kent, 1998; Hofmann, 2003). **(e)** The U-Pb age and $\varepsilon_{Hf}(t)$ values for zircon grains extracted from Meiji andesites. Zircons from Meiji dacites (Wei et al., 2021), magmatic and inherited zircons from SCB (Yang et al., 2020), and zircons from the Chimei complex of Taiwan (Shao et al., 2015) are plotted for comparison. **(f)** Relative U-Pb age probability and histogram plots of Precambrian xenocrystic/inherited zircons from igneous rocks of the eastern SCB (Wang et al., 2020).

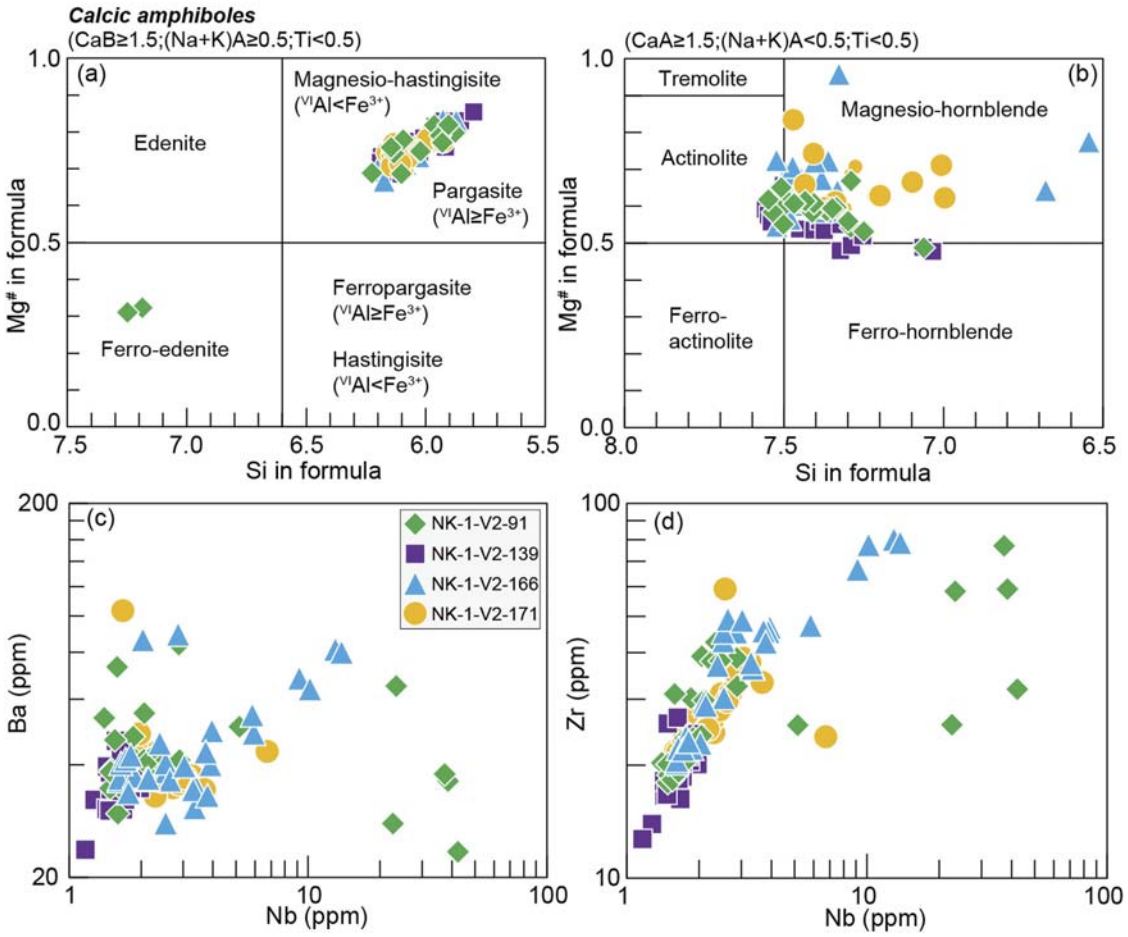

FIGURE 9
Chemical classification of the amphibole phenocrysts from the andesites after Leake et al. (1997) **(a,b)**. Amphibole trace element Nb vs. Ba **(c)** and Zr **(d)** diagrams for drilled andesites.

−5.67 to 1.31, with a T_{DM1}(Hf) from 810 Ma to 1067 Ma and T_{DM2}(Hf) from 1157 Ma to 1588 Ma. Furthermore, these andesites also show large variations in zircon $\delta^{18}O$ values from 4.0‰ to 9.0‰ (Supplementary Table S3; Figure 8b).

5 Discussion

5.1 Timing of the volcanism in Meiji Atoll

Previous geochronological studies have focused mainly on the volumes of dacites that are closely intercalated with andesites. In this study, a limited range of zircon U-Pb ages, 217.9–219.1 Ma, from dacites was believed to represent the eruption age of the volcanism (Miao et al., 2021; Wei et al., 2021). Nevertheless, the SIMS zircon U-Pb dating results from this study provide new constraints on the timing of intermediate volcanism erupted in Meiji Atoll, SCS. The older concordant $^{206}Pb/^{238}U$ zircon ages (225.6 ± 3.0 Ma), ^{207}Pb-corrected $^{206}Pb/^{238}U$ ages (223.1 ± 2.0 Ma), similar weighted mean $^{206}Pb/^{238}U$ ages (217.7 ± 2.1 Ma), and concordant $^{206}Pb/^{238}U$ ages (221.7 ± 3.6 Ma) for the formation age of andesites record a protracted volcanic history that is slightly longer than previously thought. Therefore, we consider that the volcanic rocks in the Meiji Atoll were erupted during the Late Triassic. Furthermore, the ancient inherited zircons (1898–2509 Ma) carried by the andesitic magma (sample NK-1-V2-91) shed new light on the Precambrain continental basement component within blocks in the SCS.

5.2 Petrogenesis

5.2.1 Effects of alteration, crustal assimilation, and fractional crystallization

The Meiji calc-alkaline andesites are characterized by low loss on ignition (LOI) values (0.80–1.89 wt%; Supplementary Table S2) and the fresh appearance of hand specimens, indicating that the effect of post-magmatic hydrothermal alteration on the composition of andesites is insignificant. Furthermore, the similar chondrite- and primitive mantle-normalized element patterns are also consistent with the few effects of alteration on their trace element compositions (Figure 7). The positive correlations between HFSEs (e.g., Nb, Ta, Ti, and Hf), REEs, U, Th, Y, and Zr concentrations (Figures omitted) for andesites indicate that these elements were immobile during the alteration. The Sr, Nd, Hf, and

Pb isotopic data of the Meiji calc-alkaline andesites have not been significantly disturbed by alteration, as indicated by the relatively uniform Sr, Nd, Hf, and Pb isotopic ratios and the scattered trends between LOI and Sr-Nd-Hf-Pb isotopic compositions. Therefore, HFSEs and Sr-Nd-Hf-Pb isotopic ratios can be used to reveal the primary magmatic signatures for the Meiji andesites.

Considering that these andesitic rocks travel through the continental crust before erupting to the surface, a series of low-pressure magmatic processes, including crustal contamination and fractional crystallization, might have affected the geochemical composition of the samples. The presence of inherited zircons and enrichment of Pb anomalies in primitive mantle-normalized multi-element pattern samples supports the idea that they have experienced variable crustal assimilation before eruption. Higher initial $^{87}Sr/^{86}Sr$ ratios, lower $\varepsilon_{Nd}(t)$ and $\varepsilon_{Hf}(t)$ values, higher Th/Nb ratios, and arc-like Nb-Ta depletion signatures typical of continental crust may be attributed to the involvement of crustal materials during the ascent of the magmas (Rudnick and Gao, 2013). The negative correlation between $\varepsilon_{Nd}(t)$ and $(Th/Nb)_N$ can be used to assess the degree of crustal contamination based on the observations that the Nd isotopic composition and mantle-normalized ratios are sensitive to crustal contamination (Zhang et al., 2020). However, the lack of correlation between $\varepsilon_{Nd}(t)$ and $(Th/Nb)_N$ (Figure 6e) or other crustal contamination sensitive trace ratios (La/Yb, La/Sm, and Nb/Yb) was not consistent with significant crustal contamination. The absence of any correlation between the SiO_2 contents and either $\varepsilon_{Nd}(t)$ or $\varepsilon_{Hf}(t)$ values in the Meiji Atoll lavas also indicates a lack of significant crustal contamination (Figure 6f).

Simple modeling calculations (Gan et al., 2020) for SiO_2 contents and $\varepsilon_{Nd}(t)$ values of the andesites indicate that high proportions of SCB crustal rocks (50%–60%) would be required to be added to a depleted mantle-derived melt to balance the observed element and isotope variations (Figure 6f). Such high proportions of crustal assimilation are not consistent with the relatively high $\varepsilon_{Hf}(t)$ values (−5.67 to +1.31) recorded within the zircons of andesites. Simple modeling calculations for zircon $\delta^{18}O$ and zircon $\varepsilon_{Hf}(t)$ values of the andesites (Figure 8b) also indicate that under the condition of $Hf_{pm}/Hf_c < 0.2$ (the ratio of the Hf content of the depleted mantle-derived magma over that of the crustal melt), the Hf-O isotopic compositions of most Meiji andesitic zircons can be reproduced by mixing between a depleted mantle-derived melt (ε_{Hf} = + 12, $\delta^{18}O$ = 5.3‰) and <10% crustal components (ε_{Hf} = - 12, $\delta^{18}O$ = 10‰). Consequently, the negative Nb-Ta-Ti anomalies in andesites were most likely inherited from the primary magma, indicating that the overall enrichment trends of Sr-Nd-Hf-Pb isotopes recorded in the Meiji Atoll are most likely inherited from the primary magma and controlled by the contribution of subduction components.

Lower and variable $Mg^{\#}$ (28.57–43.19), Ni (2.32–9.10 ppm), and Cr (18.4–64.7 ppm) concentrations of low-Mg andesitic lavas than those of mantle-derived primary melts ($Mg^{\#}$>68, Cr > 750 ppm and Ni > 300 ppm; Tatsumi and Ishizaka, 1982; Herzberg and O Hara, 2002) indicate that they have experienced either varying degrees of fractional crystallization of ferromagnesian minerals from a common parental magma or mixing of basaltic melts with crustal-derived melts. Despite the fact that the andesites are interbedded with dacites and basaltic rocks at different meters below sea floor (mbsf), the similarities between Sr-Nd-Hf-Pb isotopic compositions for different samples, the whole-rock trace element systematics, and major-trace element compositions of the amphibole phenocrysts suggest little evidence for magma mixing and indicate a cogenetic relationship for the four Meiji andesites. Decreases in CaO and CaO/Al_2O_3 with increasing SiO_2 in the Harker diagrams (Figures 6c,d) are consistent with clinopyroxene fractionation. The prominent Sr, Eu, and P negative anomalies in the primitive mantle-normalized trace element diagrams (Figure 7b) are likely to be associated with fractionation of plagioclase and apatite. Decreases in $Fe_2O_3^T$ and TiO_2 with increasing SiO_2 are consistent with fractional crystallization of Fe-Ti oxides. The relatively flat HREE patterns are consistent with amphibole fractionation, which is further evidenced by amphibole phenocrysts present within the samples (Figure 2). In addition, slightly to significantly negative Eu anomalies (Eu/Eu^*= 0.45–1.01) observed in the amphibole phenocrysts indicate an earlier or nearly simultaneous fractionation of plagioclases (Figures 7c,e,g).

5.2.2 Petrogenesis of the Meiji andesites

The andesites show relatively high $Mg^{\#}$ (28.57–43.19), Ni (2.32–9.10 ppm) and Cr (18.4–64.7 ppm) concentrations, distinct from those of materials or melts derived from the continental crust (e.g., Yan et al., 2010; Bai et al., 2025), indicating that these andesitic magma were likely derived from the partial melting of a mantle source. This is also supported by the observation that some zircon grains from the andesites show relatively high $\varepsilon_{Hf}(t)$ values and mantle-like O isotopic compositions ($\delta^{18}O$ = 5.3‰ ± 0.6‰). On the other hand, the andesites are calc-alkaline (Figure 5b), enriched in LILEs (e.g., Rb, Th, and U) and depleted in HFSEs (e.g., Nb, Ta, and Ti) (Figure 7b). The Nb/U ratios (8.19–31.03, average of 14) of the samples are significantly lower than those of middle ocean ridge basalt (MORB) and ocean island basalt (OIB) (Nb/U = 47; Hofmann et al., 1986) but similar to the estimates for continental arc volcanics (Nb/U = 12; Kelemen et al., 2003). The sample plot within the field of island arc calc-alkaline andesite-dacite-rhyolite on the Sr/Y vs. Y and $(La/Yb)_N$ vs. $(Yb)_N$ diagrams (Figures 5c,d), which is also consistent with abundant amphibole phenocrysts in primary hydrous magmas.

In the diagrams of chondrite-normalized rare earth element patterns and primitive mantle-normalized multi-element variation, the Meiji andesites also exhibit roughly subparallel trace element characteristics to the average continental arc andesites (Figures 7a,b). Therefore, these trace element constraints provide a strong link with subduction-related melting. In addition, these andesites display variable zircon $\delta^{18}O$ values (4.0‰–9.0‰), $\varepsilon_{Hf}(t)$ values (−5.67 to +1.31), relatively enriched whole-rock initial $^{87}Sr/^{86}Sr$ ratios (0.7083–0.7113), $\varepsilon_{Nd}(t)$ values (−6.07 to −4.91), and $\varepsilon_{Hf}(t)$ values (−7.70 to −2.16). Most of the dataset from the zircon grains in this study plots within the field of "convergent continental margins" and "arc-related/orogenic" (Figure 10), indicating a typical continental arc-related magmatism.

All these geochemical features suggest that their parental magmas were directly derived from an enriched and fertile subcontinental lithospheric mantle (SCLM) with the addition of various amounts of crustal materials via subduction. Furthermore, despite being volumetrically larger, the interbedded Meiji basaltic rocks have higher MgO, Cr, and Ni and more depleted Sr-Nd-Hf isotopic compositions than the Meiji andesites. These features, in combination with a partial melting trend on the La-La/Yb

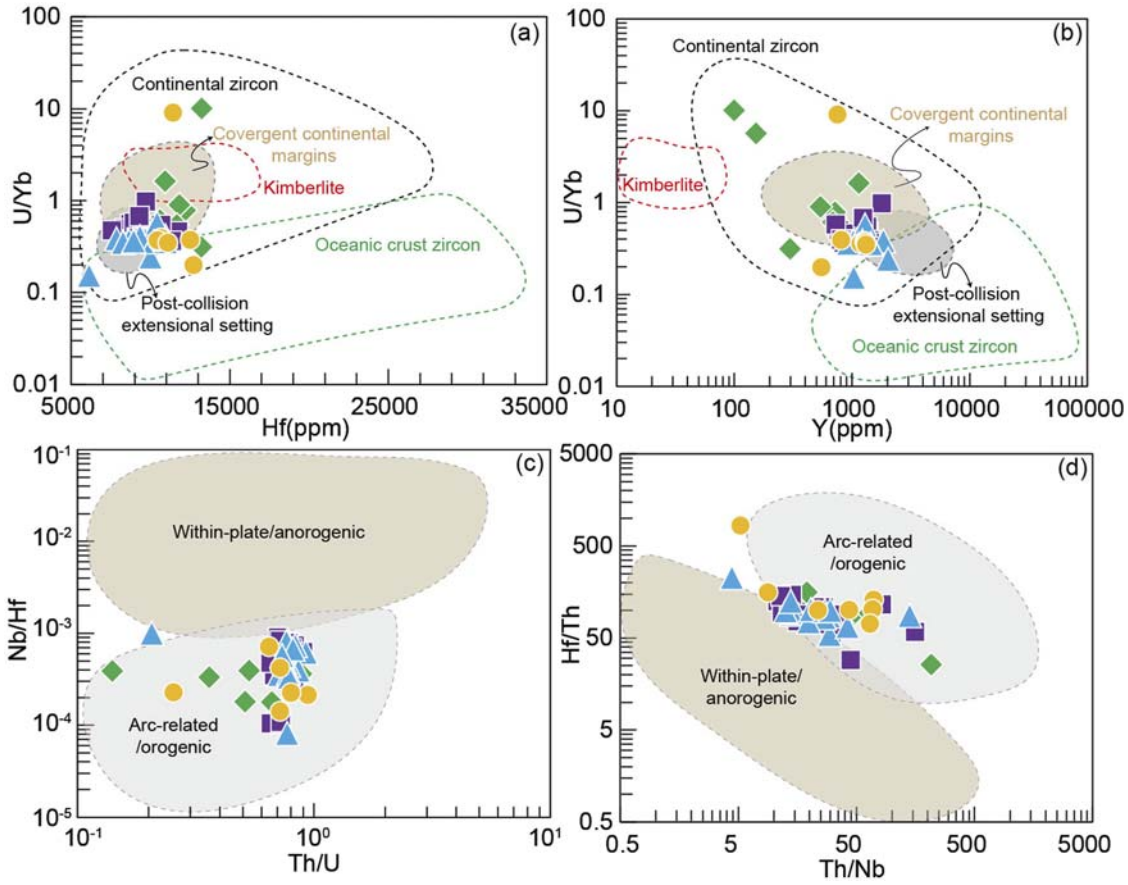

FIGURE 10
Zircon trace element **(a)** Hf vs. U/Yb (Grimes et al., 2007); **(b)** Th vs. U/Yb (Gao et al., 2013); **(c)** Th/U vs. Nb/Hf (Hawkesworth and Kemp, 2006); **(d)** Th/Nb vs. Hf/Th (Yang J. et al., 2012) diagrams for drilled andesites.

diagram (Figure 11a), preclude the possibility of a fractional crystallization relationship originating from Meiji basaltic magma. The REE concentrations and ratios have been used to constrain the composition and degree of partial melting of a mantle source. For instance, the partial melting of spinel lherzolite has little effect on the Sm/Yb ratio, but the melting in the stable field of garnet will cause a strong fractionation effect (Aldanmaz et al., 2000). The samples plot in the field of spinel to garnet transition, indicating a lherzolitic mantle source and <20% partial melting (Figure 11b). Considering that the spinel is stable at ~50–80 km depth, and garnet is stable at >80 km depth (Wyllie, 1981), it is likely that the andesites were derived from a subarc upper mantle source at depths less than 80 km.

The Meiji calc-alkaline andesites contain volumes of amphibole phenocrysts that are hydrous phases and exhibit relatively high K_2O/Na_2O ratios, implying the potential contribution of potassic phases (e.g., phlogopite and amphibole) to the composition of metasomatized lithospheric mantle (Condamine and Médard, 2014). A comparison between trace elements can be used to identify the phlogopite and amphibole mineral phase that existed in a mantle source. Due to the different incompatibilities of Rb, Ba, and Sr in phlogopite and amphibole, phlogopite- or amphibole-bearing mantle-derived melts will exhibit different Rb/Sr and Ba/Rb ratios (Späth et al., 2001). The Meiji andesites are characterized by variably low Ba/Rb (2.53–5.83) with an average of 3.82 and high Rb/Sr (0.16–0.83) ratios with an average of 0.54 (Figure 11c), indicative of phlogopite as the main potassic phase in the metasomatized mantle source, followed by breakdown of them during mantle melting. This suggestion is consistent with the K-rich rather than Na-rich feature of high-K calc-alkaline and/or shoshonitic Meiji andesites (Figure 5b), given that the presence of amphibole in the mantle source would contribute to the enrichment of Na in the resulting melt even if amphibole was not totally exhausted (Condamine and Médard, 2014).

The generation of phlogopite rather than amphibole in the metasomatic mantle domains may be to some extent caused by loss of sodium during the previous dehydration at forearc depths. These andesitic rocks display significantly more enriched radiogenic isotope compositions than common mantle-derived oceanic arc basalt. This difference implies that either their mantle sources have been aged for a long time after metasomatic formation in the subarc mantle wedge or the crustal components in the mantle sources have ancient origins (Zheng et al., 2015; Chen et al., 2018).

In general, the arc-like geochemical features recorded in these samples reveal partial melting of metasomatized lithospheric mantle modified by slab-derived hydrous fluids or sediment-derived hydrous melts. Slab-derived fluids are characterized by

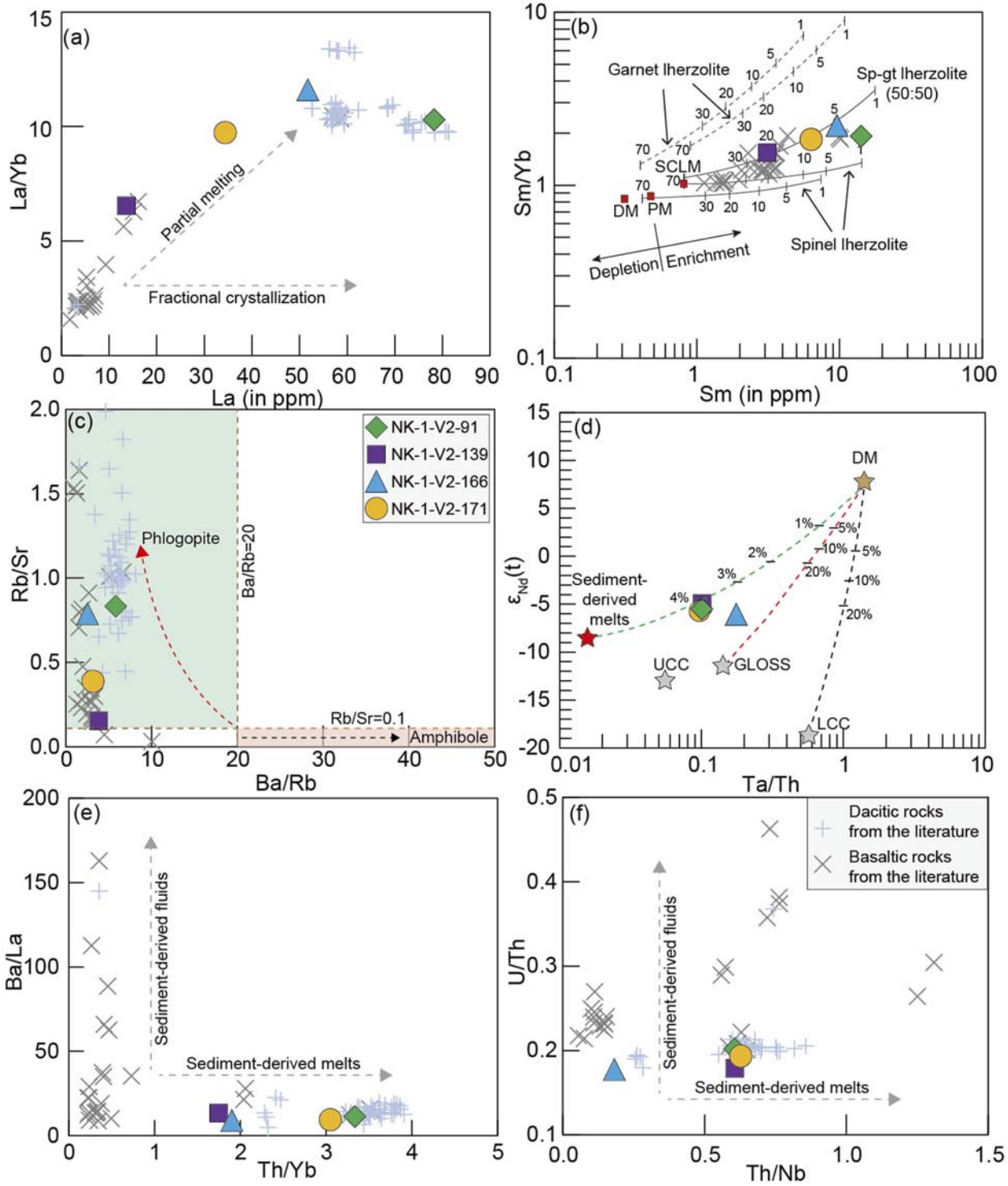

FIGURE 11
(a) La/Yb vs. La (Gan et al., 2020) and references therein. **(b)** Sm/Yb vs. Sm. The melt curves are calculated using the non-modal batch melting equations of Shaw (1970). The dashed and solid lines are melting trends of the garnet lherzolite and spinel lherzolite (DM, depleted mantle, Sm = 0.3 ppm, Sm/Yb = 0.86, Mckenzie and O'Nions, 1991; SCLM, subcontinental lithospheric mantle, Sm = 0.6 ppm, Sm/Yb = 0.96; Aldanmaz et al., 2000). Partition coefficients are from the compilation of Mckenzie and O'Nions (1991). **(c)** Rb/Sr vs. Ba/Rb (Gan et al., 2020). **(d)** $\varepsilon Nd_{(t)}$ vs. Ta/Th (Babazadeh et al., 2021). **(e)** Ba/La vs. Th/Yb. **(f)** U/Th vs. Th/Nb.

relatively high U/Th and Ba/La ratios but low Th/Yb, $(La/Sm)_N$ and Th/Nb ratios, whereas the sediment-derived melts often display relatively high Th/Yb, $(La/Sm)_N$ and Th/Nb ratios but low U/Th and Ba/La ratios (Keppler, 1996). The oceanic sediment-derived melts generally display high Th and LREEs with elevated Th/Ce ratios, whereas oceanic crust-derived melts usually show low Th/La, Th/Nb, and Th/Yb ratios (Class et al., 2000; Prouteau et al., 2001). The andesites investigated here show stronger enrichment in Th relative to U, integrated with the presence of relatively high zircon $\delta^{18}O$ values and low whole-rock and zircon $\varepsilon_{Hf}(t)$ values, which allow us to infer the involvement of sediment-derived components in the mantle source. Furthermore, the high Th/Yb (up to 3.33) and Th/Nb (up to 0.63) ratios of the samples are consistent with input from sediment-derived melts, rather than slab-derived fluids and oceanic crust-derived melts (Figures 11e,f). Modeling calculations between Ta/Th and $\varepsilon_{Nd}(t)$ also indicate that the subducted sediment components are dominated by sediment-derived melts (<5%) in the Meiji andesites (Figure 11d). Therefore, these features may imply that the Meiji calc-alkaline andesites mainly derived from a phlogopite-bearing metasomatized lithospheric mantle, which had been affected by subduction sediment compositions.

All amphibole phenocrysts from andesites show a relatively homogeneous chemical composition and consistently higher MREE over HREE in the diagram of chondrite-normalized REE pattern (Figures 7c,e,g,i), which is consistent with the partition coefficients for amphibole in an igneous process and implies a genetic link between them (Tiepolo et al., 2007). The absence of compositional zonation within amphiboles indicates fast cooling or re-equilibration at high temperature (Torres García et al., 2020). Considering the hydrothermal fluids are usually LREE-enriched (Michard, 1989), the marked depletion in LREEs (Figure 7) within these amphiboles also precludes the possibility that they are derived from interaction between an andesitic assemblage and LREE-rich aqueous fluids at subsolidus conditions.

In the primitive mantle-normalized multi-element variation diagrams (Figure 7), the LILEs (e.g., Rb, Ba, and Pb) and HFSEs (e.g., Nb, Ta, Ti, Zr, and Hf) of amphiboles exhibit a restricted range in concentrations, indicating that these elements were relatively immobile on the mineral scale. A systematic correlation between the most immobile elements (Nb) and relatively mobile (e.g., Ba) and relatively immobile elements (e.g., Zr) within the amphiboles also indicates that these elements are not significantly affected by secondary alteration and/or metamorphic disturbance (Figures 9c,d). Therefore, we can conclude that these amphibole phenocrysts likely preserve their primary igneous geochemical characteristics and record the evolutionary process at crustal depths.

5.3 Amphibole-melt thermobarometry

Thermobarometers based on Amp–melt compositions can be used to estimate the crystallization temperature and pressure of Amp in arc magmatic systems. The whole-rock compositions of andesite were assumed to be in equilibrium with the core of the Amp phenocrysts. Core compositions of Amp were used as tests for equilibrium by comparing the host-rock SiO_2 content with the result calculated for silicate liquid in equilibrium with Amp (Putirka, 2016). The Fe-Mg exchange coefficients between Amp and melt $[K_d(Fe\text{-}Mg)^{Amp\text{-}liq}]$ were employed as an additional test for the Amp–liquid pairs.

For the application of thermobarometry, we consider as suitable only core compositions from Amp crystals whose calculated melt SiO_2 differs by no more than 4.0 wt% from the SiO_2 content of the host rock (Maro et al., 2020) and the $K_d(Fe\text{-}Mg)^{Amp\text{-}liq}$ values in the range 0.28 ± 0.11 (Putirka, 2016). In the Meiji andesites, most of the Amp is in equilibrium with the respective host rocks. There are also cases where the predicted melt SiO_2 for Amp is higher or lower by 4–16.8 wt% than the host rock composition and close to that of the basaltic and dacitic lavas (Figure 12a). This may imply a probable interaction between the basaltic, dacitic, and andesitic magma during the major magma recharge event of compositionally different magma. A minimum value of 3.5 wt% for melt H_2O concentration was assumed based on the stability of magnesio-hastingsite during the P-T calculations (Ridolfi et al., 2010).

We chose the Amp-melt thermometer [Equation 5 of Putirka (2016)] to estimate the crystallization temperature of the Amp phenocrysts in this study. All suitable Amp grains from different samples yield relatively low and consistent crystallization temperatures in the range from 898 °C to 977 °C with an uncertainty of ±30 °C (Putirka, 2016). In view of the dependence of pressure on water concentrations in the melt and the poor sensitivity of Al concentrations to pressure change (Putirka, 2016; Maro et al., 2020), the pressure estimates based on amphibole equilibria should be treated with caution. Here, we use multiple barometric calibrations to place constraints on the formation of the Amp phenocrysts. We compared the results obtained by using Equation 7a of Putirka (2016), Equations 1b–d of Ridolfi and Renzulli (2012), and the formula of Ridolfi et al. (2010). The calibration of Ridolfi et al. (2010) yields pressures that correlate well with those of Ridolfi and Renzulli (2012) (Figures 12g,h), even though both the numerical agreement and the correlation of the values are worse between Equation 7a of Putirka (2016), the formula of Ridolfi et al. (2010), and Equations 1b–d of Ridolfi and Renzulli (2012) (Figures 12c–f). We consider that the Ridolfi et al. (2010) and Ridolfi and Renzulli (2012) calibration itself does not incorporate melt H_2O concentration as an explicit parameter in their calibration equation, resulting in systematic discrepancies with the H_2O-dependent thermobarometric model of Putirka (2016) in our study. Although the Amp phenocrysts in the Meiji andesites exhibit discrepancies among different barometers (Supplementary Table S6), we emphasize that these data collectively denote relatively low crystallization pressures (2–6 kbar) within the mid-upper crust levels.

The values of oxygen fugacity (fO_2) estimates following Ridolfi et al. (2010) indicate relatively oxidized magma (0.77–2.47 log units above the nickel–nickel oxide (NNO) buffer for Amp in the Meiji andesites; Figure 12b). The positive correlation between the crystallization pressure and temperature (Figures 13a,b) using different Amp–melt equilibrium geothermobarometry, integrated with relatively high fO_2, may imply a continuous and cryptic Amp fractionation during the evolution of arc magmas despite the rare occurrence of Amp as a major mineral phase in erupted volcanic rocks (Davidson et al., 2007).

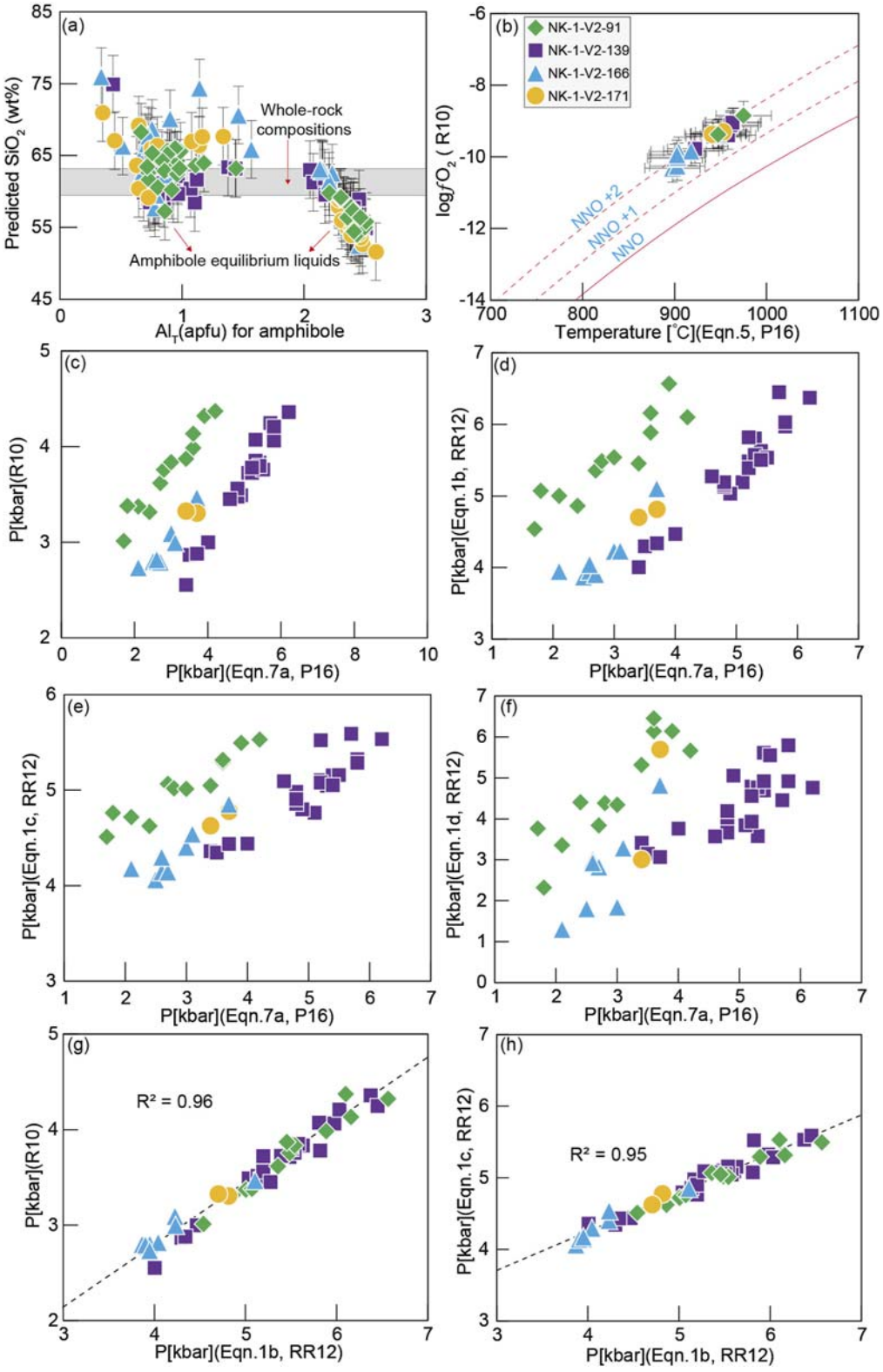

FIGURE 12
(a) Relationship between Al_{total} in amphibole and the predicted SiO_2 content of coexisting liquid. **(b)** Calculated oxygen fugacity based on amphibole compositions using the method of Ridolfi et al. (2010). **(c–h)** Comparison of amphibole barometers. Amphibole barometers between Equation 7a of Putirka (2016)and Ridolfi et al. (2010) **(c)**, Equation 1b of Ridolfi and Renzulli, (2012) **(d)**, Equation 1c of Ridolfi and Renzulli, (2012), and **(e)** Equation 1d of Ridolfi and Renzulli, (2012) **(f)**. A comparison of amphibole barometers between Equation 1b of Ridolfi and Renzulli (2012)and Ridolfi et al. (2010) **(g)** and Equation 1c of Ridolfi and Renzulli (2012) **(h)** is also shown.

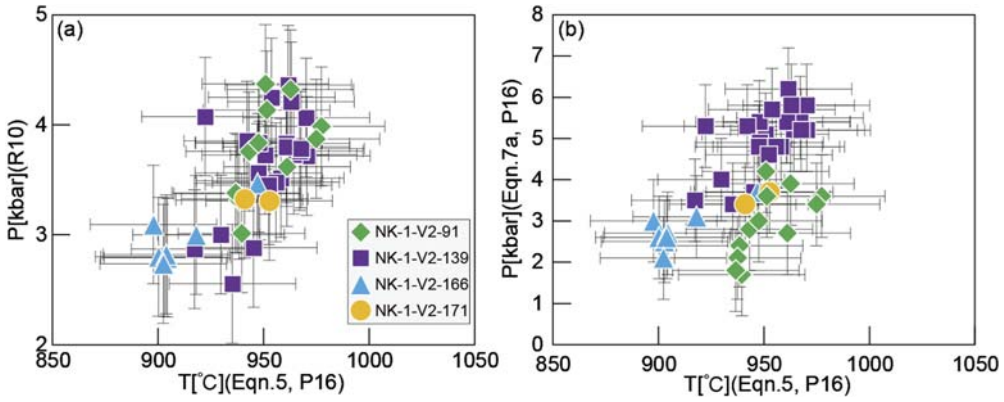

FIGURE 13
Calculated temperature and pressure based on amphibole compositions. **(a)** Using the method of Ridolfi et al. (2010) for pressure and Equation 5 of Putirka (2016) for temperature. **(b)** Using Equation 7a and Equation 5 of Putirka (2016) for pressure and temperature, respectively.

5.4 Sources of the xenocrystic/inherited zircons and basement of the Nansha Block

The identification of sources for the observed xenocrystic/inherited zircons from sample NK-1-V2-91 plays a key role in interpreting their age and exploring their geological implications. In general, various forming mechanism and sources were proposed to explain the occurrence of these xenocrystic and inherited zircons: 1) xenocrystic zircons captured by assimilation and contamination of sedimentary or igneous wall rocks during magma ascent and emplacement (Wang et al., 2020); 2) inherited zircons typically derived from intermediate and felsic host igneous rocks with sedimentary or igneous origins (e.g., S-type or I-type granites); 3) inherited zircons typically derived from SCLM modified by subducted oceanic crust-derived siliceous melts or aqueous fluids (Katayama et al., 2003; Jiang et al., 2020). Nine igneous zircons with high Th/U ratios (0.24–1.95) display $^{207}Pb/^{206}Pb$ ages much older than the magma crystallization age (218–226 Ma), indicating that they are not formed in the andesitic magma itself. Most of these old zircons are subhedral or euhedral with prismatic morphologies and fine in size (Figure 4), precluding the possibility of long-distance transport (if it happened). They also exhibit fine rhythmic zoning, indicative of zircons crystallized from intermediate-acid magmas; hence, they do not originate from a metasomatized SCLM.

The andesitic arc magma entraining these zircons was hydrous as indicated by a large amount of Amp phenocrysts, which is also not consistent with the preservation of residual zircons from mantle sources (Harrison and Watson, 1983). Exposed Archean-Proterozoic basement rocks and mantle xenoliths carrying the underlying Precambrian lithospheric relics in eastern South China require a significant amount of ancient continental crust beneath the SCB (Wang et al., 2020), which is consistent with the age patterns of the Precambrian xenocrystic/inherited zircons from SCB (Figure 8f). Therefore, the old zircon xenocrysts observed in Meiji andesites should be originated from assimilation or contamination of wall rocks during magma ascent and emplacement, as demonstrated by the result of modeling calculations for zircon $\delta^{18}O$ and zircon $\varepsilon_{Hf}(t)$ values (Figure 8f) that the Hf-O isotopic compositions of most Meiji andesitic zircons can be reproduced by mixing between a depleted mantle-derived melt (ε_{Hf} = + 12, $\delta^{18}O$ = 5.3‰) and <10% crustal components (ε_{Hf} = - 12, $\delta^{18}O$ = 10‰). They are considered advantageous for revealing the composition of the assimilated crust beneath the Nansha Block.

The Nd model ages (1776–928 Ma) for the granitic rocks from two dredge stations in the Nansha Block have been interpreted to represent the existence of a Mid-Proterozoic crystalline basement, even though the corresponding Precambrian rocks are rarely exposed in the blocks dispersed in the SCS (Yan et al., 2010). The Meiji dacites and andesites also display similar Nd model ages (1390–1537 Ma and 1477–1675 Ma) to those of Nansha granitic rocks, suggesting that the basement of the Nansha Block may preserve a residual amount of ancient crustal materials. A significant inherited zircons with ages of 1898–2509 Ma generally show negative $\varepsilon_{Hf}(t)$ (−6.3 to −1.6) except for two, 2.8 and 8.6, and a two-stage Hf model with a concentration of ages around 2623–3059 Ma, which verifies that there may have been initial crust in the Paleoproterozoic in the source area of the Nansha Block igneous rocks. These features, in combination with the extensive evidence for Precambrian basement rocks, occur in samples from other blocks of SCS that are believed to share an evolutionary history with the Nansha Block (Holloway, 1982; Kudrass et al., 1986; Hall et al., 2008; Yan et al., 2010). The identification of the oldest Cathaysia crystalline basement (the Badu Complex), including the high-grade metasedimentary rocks with a 2.5 Ga protolith (Yu et al., 2012) or a 1.9–1.8 Ga protolith (Zhao et al., 2015), and the associated 1.9–1.7 Ga granitoids and metabasic rocks (Liu et al., 2014), provides additional and compelling evidence for the existence of Paleoproterozoic crystalline basement within the Nansha Block similar to the Cathaysia Block, in view of the overlapping of the inherited zircons' U-Pb age between the Meiji andesites in this study and the igneous rocks from the eastern SCB (Figure 8f).

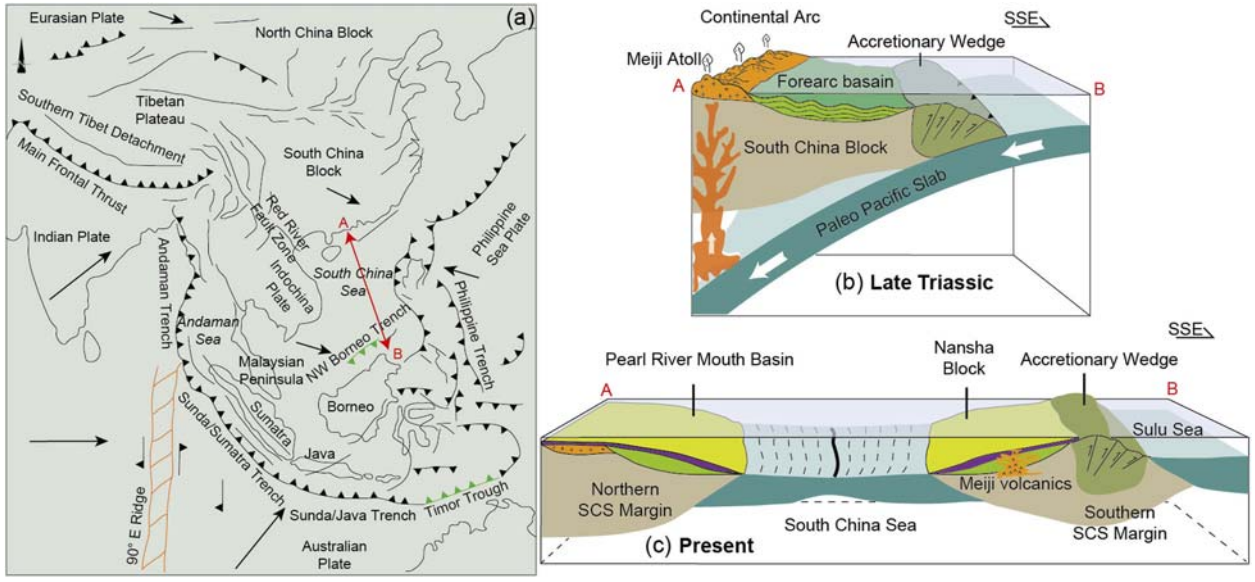

FIGURE 14
(a,c) Present-day geotectonic configuration; **(b)** Proposed Late Triassic tectonic evolution and associated arc magmatism adjacent to the South China Block. Meiji Atoll andesitic arc volcanism was produced in the South China continental margin as a result of paleo-Pacific slab subduction.

5.5 Geodynamic implications

It is well known that calc-alkaline continental arc andesites distributed at convergent margins possess a similar composition in both major and trace elements to continental crust on average (Hans Wedepohl, 1995; Rudnick and Fountain, 1995). Hence, andesitic magmatism above the oceanic subduction zone is considered to have played a significant role in the generation of continental crust along convergent plate boundaries (Kelemen, 1995; Taylor and McLennan, 1995; Grove et al., 2012; Kelemen and Behn, 2016). Andean andesites in the western margin of South America were widely accepted as the typical products of long-lived oceanic–continental convergent margins commonly named "Andean-type margins" (Hildreth and Moorbath, 1988; Davidson et al., 1990; Stern, 2004). Similarly, active continental margin and subduction-related geodynamic settings have also been inferred for the eastern and southeastern Asian margin since the late Paleozoic and early Mesozoic (Jahn et al., 1990; Zhou and Li, 2000; Li and Li, 2007; Li X.-H. et al., 2012; Metcalfe, 2013; Qiu et al., 2022). The widespread Mesozoic magmatism observed along the northern and southern (e.g., Meiji Atoll) SCS margins and the southeastern SCB demonstrates tectonic continuity between the SCS continental margin and SCB during the Mesozoic era (Qiu et al., 2014; Xu et al., 2017; Xu et al., 2022; Cui et al., 2021; Miao et al., 2021).

The andesitic arc volcanism at Meiji Atoll cannot be attributed to paleo-Tethys ocean subduction and closure, given that the Indo-China Block collided with the South China Block at 247–237 Ma, as constrained by geochronological data from the Ailaoshan–Songma suture zone rocks (Wang et al., 2013). The inferred collision (247–237 Ma) is unlikely to account for andesitic magmatism in this study as these andesites are significantly younger and were located east or southeast of the Ailaoshan–Songma suture prior to SCS basin opening. This spatial–temporal discrepancy precludes a paleo-Tethyan origin. The pre-rift paleo-position of Meiji Atoll along the SCB's coastal margin aligns with the inferred Mesozoic arc belt (Li and Li, 2007; Wei et al., 2021). In addition, paleomagnetic results revealed a >60 ° clockwise rotation of the South China Block following its Early Triassic collision with the North China Block (Zhao and Coe, 1987). This implies the Nansha Block (including Meiji Atoll), located along the SCB's southeastern coast pre-rifting, occupied an eastern position facing the paleo-Pacific during the Late Triassic.

The Late Triassic upper-section basalts and trachytes (980–1196 mbsf) from Meiji Atoll exhibit geochemical affinities with modern Mariana and Japan arc systems, providing compelling evidence for paleo-Pacific oceanic slab subduction beneath the South China margin as well (Xu et al., 2022). Consequently, the pre-rift southern SCS continental margin (including Nansha Block) was positioned along the southeastern SCB coast, dominantly controlled by paleo-Pacific plate subduction during early Mesozoic time. Once again, the drilled continental arc andesites in this study strengthen the conception of a now-vanished Andean-type convergent plate margin (Figure 14), genetically associated with subduction of the paleo-Pacific plate during the early Mesozoic and followed by growth and closure of marginal seas along the East Asia margin. Therefore, the identification of Meiji arc andesites penetrated by a borehole at the southern South China Sea continental margin shed new light on the lateral distribution and evolution of the arc system during the Late Triassic.

The buildup of this magmatic arc has been proposed to signals a major geodynamic switch from passive-margin to active-margin tectonics along the SE periphery of continental Asia, as indicated by the occurrence of 270–264 Ma ash-fall tuff layers in the Permian depositional record of SE China and widespread 267–262 Ma granitoid rocks on the island of Hainan (Li et al., 2006; Zhang et al., 2019). Additional, the remarkable change in regional

palaeogeography from a carbonate platform in Carboniferous-earliest Permian to an elongated uplift with onset of clastic deposition along the southeastern coastal regions in mid-Early Permian is also coincident with the occurrence of a prominent zircon population in the Permian sandstone and siltstone units that crop out in E-SE China (Li X.-H. et al., 2012; Hu et al., 2015; Zhang et al., 2019), implying a significant change in the geodynamic evolution along the coast of SE China. The identification of continental sliver or ribbon continent with Cathaysia-type sources in the aspect of zircon xenocrysts beneath the Gagua Ridge of Philippine Sea and eastern Taiwan (Shao et al., 2015; Qian et al., 2021), together with previously reported borehole samples in the northern SCS margin and our newly dated ca. 218–226 Ma arc andesites in the southern SCS margin (Xu et al., 2017; Cui et al., 2021; Miao et al., 2021; Wei et al., 2021), highlighting the protracted Andean-type active-margin orogenic belt over space. This Andean-type active continental margin has been proposed to experience flat-slab subduction during the Triassic (ca. 250–190 Ma), as indicated by a predicted ~1300 km-wide coastal magmatic gap (Li and Li, 2007; Li Z.-X. et al., 2012).

Following the end of the flat-slab subduction phase, a new continental arc was initiated after ca. 190 Ma, interpreted to represent the resumption of normal subduction along the coastal region (Li Z.-X. et al., 2012). In contrast, a certain number of approximately 200 Ma detrital zircons have been reported from metasedimentary borehole samples of the northern SCS basin recently, which is interpreted to reflect the close affinity of these sites to Hainan Island, which is outside of the proposed flat-slab subduction segment (Cui et al., 2021). In addition, the drilled volcanic rock series from Meiji Atoll of southern SCS was interpreted to reflect a spatial difference in distribution of arc magmatism along the SCB and possibly reveal the size of the subducted oceanic plateau (Wei et al., 2021). In combination with the Late Triassic andesites in this study, we cannot exclude the possibility that Meiji volcanic rocks, once distributed along the southern margin of the SCB, represent the earliest re-initiation of continental arc magmatism after a phase of flat-slab subduction.

6 Conclusion

SIMS zircon U-Pb dating results indicate that the andesites drilled from the Meiji Atoll of the southern South China Sea were generated during the Late Triassic (i.e., 217–226 Ma), which is consistent with previous zircon and apatite U-Pb ages. The andesitic rocks in this study are closely intercalated with dacites and basaltic rocks at different depths, suggesting that these volcanic rocks are contemporaneous and represent the Late Triassic volcanism along the southeast coast of the South China Block. Whole-rock geochemistry and trace element modeling suggest that the Meiji andesites were generated by <20% partial melting of phlogopite-bearing lherzolitic metasomatized lithospheric mantle, which had been affected by subduction sediment compositions as a response to the paleo-Pacific subduction during the Triassic. Amphibole-melt thermobarometry and mineral chemistry imply that the amphibole phenocrysts from the Meiji andesites record a continuous and cryptic amphibole fractionation confined to the upper-crustal level during the evolution of arc magmas. The old zircon xenocrysts observed in Meiji andesites originated from assimilation or contamination of wall rocks during magma ascent and emplacement, corroborating the existence of Paleoproterozoic crystalline basement beneath the Nansha Block and robust tectonic affinity with SCB. The Meiji Atoll volcanism reflects a spatial difference in the distribution of arc magmatism along the SCB or represents the earliest re-initiation of continental arc magmatism after a phase of flat-slab subduction of the paleo-Pacific.

Data availability statement

The original contributions presented in the study are included in the article/Supplementary Material; further inquiries can be directed to the corresponding author.

Author contributions

WW: Project administration, Methodology, Data curation, Conceptualization, Writing – original draft, Investigation, Writing – review and editing. C-ZL: Validation, Conceptualization, Writing – review and editing, Funding acquisition, Supervision, Investigation, Project administration, Resources, Data curation. WY: Validation, Conceptualization, Project administration, Supervision, Resources, Writing – review and editing. L-FZ: Investigation, Conceptualization, Writing – review and editing.

Funding

The author(s) declare that financial support was received for the research and/or publication of this article. This work was financially supported by the National Natural Science Foundation of China (42302064 and 42025201) and the Strategic Priority Research Program of the Chinese Academy of Sciences (XDA13010106; XDA13010102).

Acknowledgments

We thank Guo-Qiang Tang, Yu Liu, Jiao Li, Xiao-Xiao Ling, Hong-Xia Ma, and Hu Tang for the help with SIMS U-Pb dating and O isotope analyses, Wei-Qi Zhang for whole-rock trace elements analyses, Yue-Heng Yang and Ya-Zhou Feng for whole-rock Sr-Nd-Hf isotope analyses, Chao-Feng Li for whole-rock Pb isotope analyses, and Chao Huang for zircon Lu-Hf isotope analyses.

Conflict of interest

The authors declare that the research was conducted in the absence of any commercial or financial relationships that could be construed as a potential conflict of interest.

The author(s) declared that they were an editorial board member of Frontiers, at the time of submission. This had no impact on the peer review process and the final decision.

Generative AI statement

The author(s) declare that no Generative AI was used in the creation of this manuscript.

Any alternative text (alt text) provided alongside figures in this article has been generated by Frontiers with the support of artificial intelligence and reasonable efforts have been made to ensure accuracy, including review by the authors wherever possible. If you identify any issues, please contact us.

Publisher's note

Supplementary material

The Supplementary Material for this article can be found online at: https://www.frontiersin.org/articles/10.3389/feart.2025.1657965/full#supplementary-material

References

Aldanmaz, E., Pearce, J. A., Thirlwall, M. F., and Mitchell, J. G. (2000). Petrogenetic evolution of late Cenozoic, post-collision volcanism in western Anatolia, Turkey. *J. Volcanol. Geotherm. Res.* 102, 67–95. doi:10.1016/s0377-0273(00)00182-7

Anderson, A. T. (1976). Magma mixing: petrological process and volcanological tool. *J. Volcanol. Geotherm. Res.* 1, 3–33. doi:10.1016/0377-0273(76)90016-0

Annen, C., Bluddy, J. D., and Sparks, R. S. J. (2005). The genesis of intermediate and silicic magmas in deep crustal hot zones. *J. Petrology* 47, 505–539. doi:10.1093/petrology/egi084

Azizi, H., Daneshvar, N., Mohammadi, A., Asahara, Y., Whattam, S. A., Tsuboi, M., et al. (2021). Early miocene post-collision andesite in the Takab area, NW Iran. *J. Petrology* 62, egab022. doi:10.1093/petrology/egab022

Babazadeh, S., D'antonio, M., Cottle, J. M., Ghalamghash, J., Raeisi, D., and An, Y. (2021). Constraints from geochemistry, zircon U-Pb geochronology and Hf-Nd isotopic compositions on the origin of Cenozoic volcanic rocks from central Urumieh-Dokhtar magmatic arc, Iran. *Gondwana Res.* 90, 27–46. doi:10.1016/j.gr.2020.10.010

Bai, T., Qian, X., Gan, C., and Wang, Y. (2025). Late Jurassic high-silica granites in the interior and coastal South China and their tectonic implication. *Lithos* 498-499, 107971. doi:10.1016/j.lithos.2025.107971

Barry, T., and Kent, R. (1998). "Cenozoic magmatism in Mongolia and the origin of central and east Asian basalts," in *Mantle Dynamics and plate interactions in East Asia*. Editors M. F. J. Flower, S. L. Chung, C. H. Lo, and T. Y. Lee, 347–364. Washington, D. C, AUG: American Geophysical Union).

Behn, M. D., Kelemen, P. B., Hirth, G., Hacker, B. R., and Massonne, H.-J. (2011). Diapirs as the source of the sediment signature in arc lavas. *Nat. Geosci.* 4, 641–646. doi:10.1038/ngeo1214

Chen, L., and Zhao, Z.-F. (2017). Origin of continental arc andesites: the composition of source rocks is the key. *J. Asian Earth Sci.* 145, 217–232. doi:10.1016/j.jseaes.2017.04.012

Chen, L., Zheng, Y.-F., and Zhao, Z.-F. (2018). A common crustal component in the sources of bimodal magmatism: geochemical evidence from Mesozoic volcanics in the Middle-Lower Yangtze Valley, South China. *GSA Bull.* 130, 1959–1980. doi:10.1130/b31856.1

Chen, L., Zheng, Y.-F., Xu, Z., and Zhao, Z.-F. (2021). Generation of andesite through partial melting of basaltic metasomatites in the mantle wedge: Insight from quantitative study of Andean andesites. *Geosci. Front.* 12, 101124. doi:10.1016/j.gsf.2020.12.005

Class, C., Miller, D. M., Goldstein, S. L., and Langmuir, C. H. (2000). Distinguishing melt and fluid subduction components in Umnak volcanics, Aleutian arc. *Geochem. Geophys. Geosystems* 1. doi:10.1029/1999gc000010

Codillo, E. A., Le Roux, V., and Marschall, H. R. (2018). Arc-like magmas generated by mélange-peridotite interaction in the mantle wedge. *Nat. Commun.* 9, 2864. doi:10.1038/s41467-018-05313-2

Condamine, P., and Médard, E. (2014). Experimental melting of phlogopite-bearing mantle at 1 GPa: implications for potassic magmatism. *Earth Planet. Sci. Lett.* 397, 80–92. doi:10.1016/j.epsl.2014.04.027

Cui, Y., Shao, L., Li, Z.-X., Zhu, W., Qiao, P., and Zhang, X. (2021). A Mesozoic Andean-type active continental margin along coastal South China: new geological records from the basement of the northern South China Sea. *Gondwana Res.* 99, 36–52. doi:10.1016/j.gr.2021.06.021

Davidson, J. P., Mcmillan, N. J., Moorbath, S., Wörner, G., Harmon, R. S., and Lopez-Escobar, L. (1990). The Nevados de Payachata volcanic region (18 °S/69 °W, N. Chile) II. Evidence for widespread crustal involvement in Andean magmatism. *Contributions Mineralogy Petrology* 105, 412–432. doi:10.1007/bf00286829

Davidson, J., Turner, S., Handley, H., Macpherson, C., and Dosseto, A. (2007). Amphibole "sponge" in arc crust? *Geology* 35, 787–790. doi:10.1130/g23637a.1

Feng, Y., Yang, J., Sun, J., and Zhang, J. (2020). Material records for Mesozoic destruction of the North China Craton by subduction of the paleo-Pacific slab. *Sci. China Earth Sci.* 63, 690–700. doi:10.1007/s11430-019-9564-4

Gan, C., Wang, Y., Barry, T. L., Zhang, Y., and Qian, X. (2020). Late Jurassic high-Mg andesites in the Youjiang basin and their significance for the southward continuation of the Jiangnan orogen, south China. *Gondwana Res.* 77, 260–273. doi:10.1016/j.gr.2019.06.018

Gao, Q., Zhang, N., Xia, W., Feng, Q., Chen, Z.-Q., Zheng, J., et al. (2013). Origin of volcanic ash beds across the Permian–Triassic boundary, Daxiakou, South China: Petrology and U–Pb age, trace elements and Hf-isotope composition of zircon. *Chem. Geol.* 360-361, 41–53. doi:10.1016/j.chemgeo.2013.09.020

Gómez-Tuena, A., Cavazos-Tovar, J. G., Parolari, M., Straub, S. M., and Espinasa-Pereña, R. (2018). Geochronological and geochemical evidence of continental crust 'relamination' in the origin of intermediate arc magmas. *Lithos* 322, 52–66. doi:10.1016/j.lithos.2018.10.005

Griffin, W. L., Powell, W. J., Pearson, N. J., and O'reilly, S. (2008). "GLITTER: data reduction software for laser ablation ICP-MS," in *Laser ablation ICP-MS in the earth Sciences: current practices outstanding issues*. Editor P. Sylvester. Quebec, Canada: (Mineralogical Association of Canada Short Course), 308–311.

Grimes, C. B., John, B. E., Kelemen, P. B., Mazdab, F. K., Wooden, J. L., Cheadle, M. J., et al. (2007). Trace element chemistry of zircons from oceanic crust: a method for distinguishing detrital zircon provenance. *Geology* 35, 643–646. doi:10.1130/g23603a.1

Grove, T. L., Till, C. B., and Krawczynski, M. J. (2012). The role of H2O in subduction zone magmatism. *Annu. Rev. Earth Planet. Sci.* 40, 413–439. doi:10.1146/annurev-earth-042711-105310

Hall, R., Van Hattum, M. W. A., and Spakman, W. (2008). Impact of India–Asia collision on SE Asia: the record in Borneo. *Tectonophysics* 451, 366–389. doi:10.1016/j.tecto.2007.11.058

Hans Wedepohl, K. (1995). The composition of the continental crust. *Geochimica Cosmochimica Acta* 59, 1217–1232. doi:10.1016/0016-7037(95)00038-2

Harrison, T. M., and Watson, E. B. (1983). Kinetics of zircon dissolution and zirconium diffusion in granitic melts of variable water content. *Contributions Mineralogy Petrology* 84, 66–72. doi:10.1007/bf01132331

Hart, S. R. (1984). A large-scale isotope anomaly in the Southern Hemisphere mantle. *Nature* 309, 753–757. doi:10.1038/309753a0

Hastie, A., Kerr, A., Pearce, J., and Mitchell, S. (2007). Classification of altered volcanic island arc rocks using immobile trace elements: development of the Th Co discrimination diagram. *J. Petrology* 48, 2341–2357. doi:10.1093/petrology/egm062

Hawkesworth, C. J., and Kemp, A. I. S. (2006). Using hafnium and oxygen isotopes in zircons to unravel the record of crustal evolution. *Chem. Geol.* 226, 144–162. doi:10.1016/j.chemgeo.2005.09.018

Hayes, D. E., and Nissen, S. S. (2005). The South China sea margins: implications for rifting contrasts. *Earth Planet. Sci. Lett.* 237, 601–616. doi:10.1016/j.epsl.2005.06.017

Herzberg, C., and O Hara, M. (2002). Plume-associated Ultramafic magmas of Phanerozoic age. *J. Petrology* 43, 1857–1883. doi:10.1093/petrology/43.10.1857

Hildreth, W., and Moorbath, S. (1988). Crustal contributions to arc magmatism in the Andes of Central Chile. *Contributions Mineralogy Petrology* 98, 455–489. doi:10.1007/bf00372365

Hirose, K. (1997). Melting experiments on lherzolite KLB-1 under hydrous conditions and generation of high-magnesian andesitic melts. *Geology* 25, 42–44. doi:10.1130/0091-7613(1997)025<0042:meolku>2.3.co;2

Hofmann, A. (2003). Sampling mantle heterogeneity through oceanic basalts: isotopes and trace elements. *Treatise Geochem.* 2, 568. doi:10.1016/B0-08-043751-6/02123-X

Hofmann, A. W., Jochum, K. P., Seufert, M., and White, W. M. (1986). Nb and Pb in oceanic basalts: new constraints on mantle evolution. *Earth Planet. Sci. Lett.* 79, 33–45. doi:10.1016/0012-821x(86)90038-5

Holloway, N. H. (1982). North Palawan block, Philippines–Its relation to Asian Mainland and role in evolution of South China sea. *Am. Assoc. Petroleum Geol. Bull.* 66, 1355–1383. doi:10.1306/03b5a7a5-16d1-11d7-8645000102c1865d

Hu, L., Cawood, P. A., Du, Y., Yang, J., and Jiao, L. (2015). Late Paleozoic to early Mesozoic provenance record of paleo-Pacific subduction beneath south China. *Tectonics* 34, 986–1008. doi:10.1002/2014tc003803

Huang, W., and Wang, P. (2006). Sediment mass and distribution in the South China sea since the Oligocene. *Sci. China Ser. D Earth Sci.* 49, 1147–1155. doi:10.1007/s11430-006-2019-4

Jackson, M. D., Cheadle, M. J., and Atherton, M. P. (2003). Quantitative modeling of granitic melt generation and segregation in the continental crust. *J. Geophys. Res.* 108. doi:10.1029/2001jb001050

Jahn, B.-M., Zhou, X. H., and Li, J. L. (1990). Formation and tectonic evolution of southeastern China and Taiwan: isotopic and geochemical constraints. *Tectonophysics* 183, 145–160. doi:10.1016/0040-1951(90)90413-3

Jiang, C.-H., Wang, X.-L., Wang, S., Du, D.-H., Huang, Y., Zhang, Y.-Z., et al. (2020). Paleoproterozoic basement beneath the Eastern Cathaysia Block revealed by zircon xenocrysts from late Mesozoic volcanics. *Precambrian Res.* 350, 105922. doi:10.1016/j.precamres.2020.105922

Jiao, S.-J., Li, X.-H., Huang, H.-Q., and Deng, X.-G. (2015). Metasedimentary melting in the formation of charnockite: petrological and zircon U-Pb-Hf-O isotope evidence from the Darongshan S-type granitic complex in southern China. *Lithos* 239, 217–233. doi:10.1016/j.lithos.2015.10.004

Katayama, I., Muko, A., Iizuka, T., Maruyama, S., Terada, K., Tsutsumi, Y., et al. (2003). Dating of zircon from Ti-clinohumite–bearing garnet peridotite: implication for timing of mantle metasomatism. *Geology* 31, 713–716. doi:10.1130/g19525.1

Kelemen, P. B. (1995). Genesis of high Mg# andesites and the continental crust. *Contributions Mineralogy Petrology* 120, 1–19. doi:10.1007/s004100050054

Kelemen, P. B., and Behn, M. D. (2016). Formation of lower continental crust by relamination of buoyant arc lavas and plutons. *Nat. Geosci.* 9, 197–205. doi:10.1038/ngeo2662

Kelemen, P. B., Hanghøj, K., and Greene, A. R. (2003). One view of the geochemistry of subduction-related magmatic arcs, with an Emphasis on primitive andesite and lower crust. *Treatise Geochem.* 3, 593–659. doi:10.1016/B0-08-043751-6/03035-8

Kelemen, P., Hanghøj, K., and Greene, A. (2007). One view of the geochemistry of subduction-related magmatic arcs, with an Emphasis on primitive andesite and lower crust. *Treatise Geochem.* 3, 749–806. doi:10.1016/b978-0-08-095975-7.00323-5

Kelley, K. A., Plank, T., Farr, L., Ludden, J., and Staudigel, H. (2005). Subduction cycling of U, Th, and Pb. *Earth Planet. Sci. Lett.* 234, 369–383. doi:10.1016/j.epsl.2005.03.005

Kent, A. J. R., Darr, C., Koleszar, A. M., Salisbury, M. J., and Cooper, K. M. (2010). Preferential eruption of andesitic magmas through recharge filtering. *Nat. Geosci.* 3, 631–636. doi:10.1038/ngeo924

Keppler, H. (1996). Constraints from partitioning experiments on the composition of subduction-zone fluids. *Nature* 380, 237–240. doi:10.1038/380237a0

Kudrass, H. R., Wiedicke, M., Cepek, P., Kreuzer, H., and Müller, P. (1986). Mesozoic and Cainozoic rocks dredged from the South China sea (Reed Bank area) and Sulu Sea and their significance for plate-tectonic reconstructions. *Mar. Petroleum Geol.* 3, 19–30. doi:10.1016/0264-8172(86)90053-x

Leake, B. E., Woolley, A. R., Arps, C. E. S., Birch, W. D., Gilbert, M. C., Grice, J. D., et al. (1997). Nomenclature of amphiboles: Report of the subcommittee on amphiboles of the international mineralogical association, commission on new minerals and mineral names. *Can. Mineral.* 35, 219–246.

Lee, C.-T. A., and Bachmann, O. (2014). How important is the role of crystal fractionation in making intermediate magmas? Insights from Zr and P systematics. *Earth Planet. Sci. Lett.* 393, 266–274. doi:10.1016/j.epsl.2014.02.044

Li, Z. X., and Li, X. H. (2007). Formation of the 1300-km-wide intracontinental orogen and postorogenic magmatic province in Mesozoic South China: a flat-slab subduction model. *Geology* 35, 179–182. doi:10.1130/g23193a.1

Li, X.-H., Li, Z.-X., Li, W.-X., and Wang, Y. J. T. J. O. G. (2006). Initiation of the Indosinian orogeny in south China: evidence for a Permian magmatic arc on Hainan island. *J. Geol.* 114, 341–353. doi:10.1086/501222

Li, X.-H., Liu, Y., Li, Q.-L., Guo, C.-H., and Chamberlain, K. R. (2009a). Precise determination of Phanerozoic zircon Pb/Pb age by multicollector SIMS without external standardization. *Geochem. Geophys. Geosyst.* 10, Q04010. doi:10.1029/2009gc002400

Li, X., Li, W., Wang, X., Li, Q., Liu, Y., and Tang, G. (2009b). Role of mantle-derived magma in genesis of early Yanshanian granites in the Nanling Range, South China: *in situ* zircon Hf-O isotopic constraints. *Sci. China Ser. D Earth Sci.* 52, 1262–1278. doi:10.1007/s11430-009-0117-9

Li, X.-H., Long, G., Li, Q., Liu, Y., Zheng, Y.-F., Yang, Y., et al. (2010). Penglai zircon Megacrysts: a potential new working reference material for Microbeam determination of Hf–O isotopes and U–Pb age. *Geostand. Geoanalytical Res.* 34, 117–134. doi:10.1111/j.1751-908x.2010.00036.x

Li, X.-H., Li, Z. X., He, B., Li, W.-X., Li, Q., Gao, Y., et al. (2012a). The Early Permian active continental margin and crustal growth of the Cathaysia Block: *in situ* U–Pb, Lu–Hf and O isotope analyses of detrital zircons. *Chem. Geol.* 328, 195–207. doi:10.1016/j.chemgeo.2011.10.027

Li, Z.-X., Li, X.-H., Chung, S.-L., Lo, C.-H., Xu, X., and Li, W.-X. (2012b). Magmatic switch-on and switch-off along the South China continental margin since the Permian: transition from an Andean-type to a western Pacific-type plate boundary. *Tectonophysics* 532, 271–290. doi:10.1016/j.tecto.2012.02.011

Li, B., Zhao, K. D., Yang, S. Y., and Dai, B. Z. (2013). Petrogenesis of the porphyritic dacite from Ermiaogou Cu-Au deposit in Zijinshan ore field and its metallogenetic implications. *Acta Petrol. Sin.* 12, 4167–4185. (in Chinese with English abstract).

Li, C. F., Chu, Z. Y., Guo, J. H., Li, Y. L., Yang, Y. H., and Li, X. H. J. a.M. (2015). A rapid single column separation scheme for high-precision Sr-Nd-Pb isotopic analysis in geological samples using thermal ionization mass spectrometry. *Anal. Methods* 7, 4793–4802. doi:10.1039/c4ay02896a

Li, Y., Huang, H., Grevemeyer, I., Qiu, X., Zhang, H., and Wang, Q. (2021). Crustal structure beneath the Zhongsha Block and the adjacent abyssal basins, South China Sea: new insights into rifting and initiation of seafloor spreading. *Gondwana Res.* 99, 53–76. doi:10.1016/j.gr.2021.06.015

Liu, Q., Yu, J.-H., O'reilly, S. Y., Zhou, M.-F., Griffin, W. L., Wang, L., et al. (2014). Origin and geological significance of Paleoproterozoic granites in the northeastern Cathaysia block, south China. *Precambrian Res.* 248, 72–95. doi:10.1016/j.precamres.2014.04.001

Ludwig, K. (2000). *Users manual for Isoplot/Ex: a geochronological toolkit for Microsoft Excel*, 1a. Berkeley Geochronology Center Spec. Publ., 53.

Maro, G., Trumbull, R. B., Caffe, P. J., Jofré, C. B., Filipovich, R. E., and Frick, D. A. (2020). The composition of amphibole phenocrysts in Neogene mafic volcanic rocks from the Puna plateau: insights on the evolution of hydrous back-arc magmas. *Lithos* 376-377, 105738. doi:10.1016/j.lithos.2020.105738

Mckenzie, D., and O'Nions, R. K. (1991). Partial melt distributions from Inversion of rare earth element concentrations. *J. Petrology* 32, 1021–1091. doi:10.1093/petrology/32.5.1021

Metcalfe, I. (2013). Gondwana dispersion and Asian accretion: tectonic and palaeogeographic evolution of eastern Tethys. *J. Asian Earth Sci.* 66, 1–33. doi:10.1016/j.jseaes.2012.12.020

Miao, X.-Q., Huang, X.-L., Yan, W., Yang, F., Zhang, W.-F., Cai, Y.-X., et al. (2021). Late Triassic dacites from well NK-1 in the Nansha block: constraints on the Mesozoic tectonic evolution of the southern South China sea margin. *Lithos* 398-399, 106337. doi:10.1016/j.lithos.2021.106337

Michard, A. (1989). Rare earth element systematics in hydrothermal fluids. *Geochimica Cosmochimica Acta* 53, 745–750. doi:10.1016/0016-7037(89)90017-3

Miller, D. J., and Christensen, N. L. (1994). Seismic signature and geochemistry of an island arc: a multidisciplinary study of the Kohistan accreted terrane, northern Pakistan. *J. Geophys. Res. Solid Earth* 99, 11623–11642. doi:10.1029/94jb00059

Mitchell, A. L., and Grove, T. L. (2015). Melting the hydrous, subarc mantle: the origin of primitive andesites. *Contributions Mineralogy Petrology* 170, 13. doi:10.1007/s00410-015-1161-4

Nielsen, S., and Marschall, H. (2017). Geochemical evidence for mélange melting in global arcs. *Sci. Adv.* 3, e1602402. doi:10.1126/sciadv.1602402

Plank, T., and Langmuir, C. H. (1998). The chemical composition of subducting sediment and its consequences for the crust and mantle. *Chem. Geol.* 145, 325–394. doi:10.1016/s0009-2541(97)00150-2

Prouteau, G., Scaillet, B., Pichavant, M., and Maury, R. (2001). Evidence for mantle metasomatism by hydrous silicic melts derived from subducted oceanic crust. *Nature* 410, 197–200. doi:10.1038/35065583

Putirka, K. (2016). Special Collection: Rates and Depths of Magma Ascent on Earth: amphibole thermometers and barometers for igneous systems and some implications for eruption mechanisms of felsic magmas at arc volcanoes. *Am. Mineralogist* 101, 841–858. doi:10.2138/am-2016-5506

Qian, S., Zhang, X., Wu, J., Lallemand, S., Nichols, A. R. L., Huang, C., et al. (2021). First identification of a Cathaysian continental fragment beneath the Gagua Ridge, Philippine Sea, and its tectonic implications. *Geology* 49, 1332–1336. doi:10.1130/g48956.1

Qiu, L., Yan, D.-P., Zhou, M.-F., Arndt, N. T., Tang, S.-L., and Qi, L. (2014). Geochronology and geochemistry of the Late Triassic Longtan pluton in South China: termination of the crustal melting and Indosinian orogenesis. *Int. J. Earth Sci.* 103, 649–666. doi:10.1007/s00531-013-0996-z

Qiu, L., Kong, R., Yan, D.-P., Mu, H.-X., Sun, W., Sun, S., et al. (2022). Paleo–Pacific plate subduction on the eastern Asian margin: insights from the Jurassic foreland system of the overriding plate. *GSA Bull.* 134, 2305–2320. doi:10.1130/b36118.1

Ridolfi, F., and Renzulli, A. (2012). Calcic amphiboles in calc-alkaline and alkaline magmas: thermobarometric and chemometric empirical equations valid up to 1,130 °C and 2.2 GPa. *Contributions Mineralogy Petrology* 163, 877–895. doi:10.1007/s00410-011-0704-6

Ridolfi, F., Renzulli, A., and Puerini, M. (2010). Stability and chemical equilibrium of amphibole in calc-alkaline magmas: an overview, new thermobarometric formulations and application to subduction-related volcanoes. *Contributions Mineralogy Petrology* 160, 45–66. doi:10.1007/s00410-009-0465-7

Ros, E., Pérez-Gussinyé, M., Araújo, M., Thoaldo Romeiro, M., Andrés-Martínez, M., and Morgan, J. P. (2017). Lower crustal strength controls on melting and Serpentinization at magma-poor margins: potential implications for the South Atlantic. *Geochem. Geophys. Geosyst* 18, 4538–4557. doi:10.1002/2017gc007212

Rudnick, R. L., and Fountain, D. M. (1995). Nature and composition of the continental crust: a lower crustal perspective. *Rev. Geophys* 33, 267–309. doi:10.1029/95rg01302

Rudnick, R., and Gao, S. (2013). Composition of the continental crust. *Treatise Geochem.* 4, 1–51. doi:10.1016/b978-0-08-095975-7.00301-6

Savva, D., Pubellier, M., Franke, D., Chamot-Rooke, N., Meresse, F., Steuer, S., et al. (2014). Different expressions of rifting on the South China Sea margins. *Mar. Petroleum Geol.* 58, 579–598. doi:10.1016/j.marpetgeo.2014.05.023

Shao, W.-Y., Chung, S.-L., Chen, W.-S., Lee, H.-Y., and Xie, L.-W. (2015). Old continental zircons from a young oceanic arc, eastern Taiwan: implications for Luzon subduction initiation and Asian accretionary orogeny. *Geology* 43, 479–482. doi:10.1130/g36499.1

Shaw, D. M. (1970). Trace element fractionation during anatexis. *Geochimica Cosmochimica Acta* 34, 237–243. doi:10.1016/0016-7037(70)90009-8

Sisson, T. W., and Grove, T. L. (1993). Experimental investigations of the role of H2O in calc-alkaline differentiation and subduction zone magmatism. *Contributions Mineralogy Petrology* 113, 143–166. doi:10.1007/bf00283225

Smith, D. R., and Leeman, W. P. (1987). Petrogenesis of mount St. HElens dacitic magmas. *J. Geophys. Res. Solid Earth* 92, 10313–10334. doi:10.1029/jb092ib10p10313

Späth, A., Le Roex, A. P., and Opiyo-Akech, N. (2001). Plume-lithosphere interaction and the origin of continental rift-related alkaline volcanism- the Chyulu Hills Volcanic province, Southern Kenya. *J. Petrology* 42, 765–787. doi:10.1093/petrology/42.4.765

Stern, C. R. (2004). Active Andean volcanism: its geologic and tectonic setting. *Rev. Geol.* 31, 161–206. doi:10.4067/s0716-02082004000200001

Straub, S. M., Lagatta, A. B., Martin-Del Pozzo, A. L., and Langmuir, C. H. (2008). Evidence from high-Ni olivines for a hybridized peridotite/pyroxenite source for orogenic andesites from the central Mexican Volcanic Belt. *Geochem. Geophys. Geosyst* 9. doi:10.1029/2007gc001583

Straub, S. M., Gomez-Tuena, A., Stuart, F. M., Zellmer, G. F., Espinasa-Perena, R., Cai, Y., et al. (2011). Formation of hybrid arc andesites beneath thick continental crust. *Earth Planet. Sci. Lett.* 303, 337–347. doi:10.1016/j.epsl.2011.01.013

Sun, S.-S., and Mcdonough, W. F. (1989). *Chemical and isotopic systematics of oceanic basalts: implications for mantle composition and processes*, 42. London, Special Publications: Geological Society, 313–345.

Sun, Z., Lin, J., Qiu, N., Jian, Z., Wang, P., Pang, X., et al. (2019). The role of magmatism in the thinning and breakup of the South China Sea continental margin: Special topic: the South China sea ocean drilling. *Natl. Sci. Rev.* 6, 871–876. doi:10.1093/nsr/nwz116

Tamura, Y., Sato, T., Fujiwara, T., Kodaira, S., and Nichols, A. (2016). Advent of continents: a new Hypothesis. *Sci. Rep.* 6, 33517. doi:10.1038/srep33517

Tang, X., Chen, L., Hu, S., Yang, S., Zhang, G., Shen, H., et al. (2014). Tectono-thermal evolution of the Reed Bank basin, southern South China sea. *J. Asian Earth Sci.* 96, 344–352. doi:10.1016/j.jseaes.2014.09.030

Taniuchi, H., Kuritani, T., and Nakagawa, M. (2020). Generation of calc-alkaline andesite magma through crustal melting induced by emplacement of mantle-derived water-rich primary magma: evidence from Rishiri Volcano, southern Kuril Arc. *Lithos* 354-355, 105362. doi:10.1016/j.lithos.2019.105362

Tatsumi, Y., and Ishizaka, K. (1982). Origin of high-magnesian andesites in the Setouchi volcanic belt, southwest Japan, I. Petrographical and chemical characteristics. *Earth Planet. Sci. Lett.* 60, 293–304. doi:10.1016/0012-821x(82)90008-5

Tatsumi, Y., Takahashi, T., Hirahara, Y., Chang, Q., Miyazaki, T., Kimura, J.-I., et al. (2008). New insights into andesite genesis: the role of mantle-derived calc-alkalic and crust-derived Tholeiitic melts in magma differentiation beneath Zao volcano, NE Japan. *J. Petrology* 49, 1971–2008. doi:10.1093/petrology/egn055

Taylor, S. R. (1967). The origin and growth of continents. *Tectonophysics* 4, 17–34. doi:10.1016/0040-1951(67)90056-x

Taylor, B., and Hayes, D. (1983). "Origin and history of the South China sea basin," in *The tectonic and geologic evolution of the southeast Asian seas and islands: Part 2*. Editor D. E. Hayes (Washington, DC: American Geophysical Union Geophysical Monograph Series), 23–56.

Taylor, S. R., and Mclennan, S. M. (1995). The geochemical evolution of the continental crust. *Rev. Geophys* 33, 241–265. doi:10.1029/95rg00262

Tiepolo, M., Oberti, R., Zanetti, A., Vannucci, R., and Foley, S. F. (2007). "Trace-element partitioning between amphibole and silicate melt," in *Reviews in Mineralogy and geochemistry*.

Torres García, M. F., Calderón, M., Ramírez De Arellano, C., Hervé, F., Opitz, J., Theye, T., et al. (2020). Trace element composition of amphibole and petrogenesis of hornblendites and plutonic suites of Cretaceous magmatic arcs developed in the Fuegian Andes, southernmost South America. *Lithos* 372-373, 105656. doi:10.1016/j.lithos.2020.105656

Vervoort, J. D., Plank, T., and Prytulak, J. (2011). The Hf–Nd isotopic composition of marine sediments. *Geochimica Cosmochimica Acta* 75, 5903–5926. doi:10.1016/j.gca.2011.07.046

Wang, Y., Fan, W., Cawood, P. A., and Li, S. (2008). Sr–Nd–Pb isotopic constraints on multiple mantle domains for Mesozoic mafic rocks beneath the South China Block hinterland. *Lithos* 106, 297–308. doi:10.1016/j.lithos.2008.07.019

Wang, Y., Fan, W., Zhang, G., and Zhang, Y. (2013). Phanerozoic tectonics of the South China block: key observations and controversies. *Gondwana Res.* 23, 1273–1305. doi:10.1016/j.gr.2012.02.019

Wang, K., Dong, S., Yao, W., Zhang, Y., Li, J., Cui, J., et al. (2020). Xenocrystic/inherited Precambrian zircons entrained within igneous rocks from eastern South China: Tracking unexposed ancient crust and implications for late Paleoproterozoic orogenesis. *Gondwana Res.* 84, 194–210. doi:10.1016/j.gr.2020.02.015

Wei, W., Liu, C.-Z., Hou, Y.-F., Deng, C.-L., Yan, W., Li, X.-H., et al. (2021). Discovery of a hidden Triassic arc in the southern South China sea: evidence for the breakaway of a ribbon continent with implications for the evolution of the western Pacific margin. *Terra Nova n/a* 34, 12–19. doi:10.1111/ter.12556

Winchester, J., and Floyd, P. (1976). Geochemical magma type discrimination: application to altered and metamorphosed basic igneous rocks. *Earth Planet. Sci. Lett.* 28, 459–469. doi:10.1016/0012-821x(76)90207-7

Winchester, J. A., and Floyd, P. A. (1977). Geochemical discrimination of different magma series and their differentiation products using immobile elements. *Chem. Geol.* 20, 325–343. doi:10.1016/0009-2541(77)90057-2

Woodhead, J., and Hergt, J. (2007). A Preliminary Appraisal of Seven natural zircon reference materials for *in situ* Hf isotope determination. *Geostand. Geoanalytical Res.* 29, 183–195. doi:10.1111/j.1751-908x.2005.tb00891.x

Wu, F.-Y., Yang, Y., Xie, L., Yang, J.-H., and Xu, P. (2006). Hf isotopic compositions of the standard zircons and baddeleyites used in U-Pb geochronology. *Chem. Geol.* 234, 105–126. doi:10.1016/j.chemgeo.2006.05.003

Wu, S., Karius, V., Schmidt, B. C., Simon, K., and Wörner, G. (2018). Comparison of Ultrafine powder Pellet and Flux-free fusion glass for bulk analysis of granitoids by laser ablation-inductively coupled plasma-mass spectrometry. *Geostand. Geoanalytical Res.* 42, 575–591. doi:10.1111/ggr.12230

Wu, S., Wörner, G., Jochum, K. P., Stoll, B., Simon, K., and Kronz, A. (2019). The Preparation and Preliminary Characterisation of three synthetic andesite reference glass materials (ARM-1, ARM-2, ARM-3) for *in situ* microanalysis. *Geostand. Geoanalytical Res.* 43, 567–584. doi:10.1111/ggr.12301

Wyllie, P. J. (1981). Plate tectonics and magma genesis. *Geol. Rundsch.* 70, 128–153. doi:10.1007/bf01764318

Xie, X., Xu, X., Zou, H., Jiang, S., Zhang, M., and Qiu, J. (2006). Early J2 basalts in SE China: Incipience of large-scale late Mesozoic magmatism. *Sci. China Ser. D Earth Sci.* 49, 796–815. doi:10.1007/s11430-006-0796-4

Xie, L., Zhang, Y., Zhang, H., Sun, J., and Wu, F. (2008). *In situ* simultaneous determination of trace elements, U-Pb and Lu-Hf isotopes in zircon and baddeleyite. *Chin. Sci. Bull.* 53, 1565–1573. doi:10.1007/s11434-008-0086-y

Xu, C., Zhang, L., Shi, H., Brix, M. R., Huhma, H., Chen, L., et al. (2017). Tracing an early Jurassic magmatic arc from south to east China seas. *Tectonics* 36, 466–492. doi:10.1002/2016tc004446

Xu, F., Zhang, G., Yan, W., Zhang, J., and Yao, J. (2022). Subduction of the paleo-Pacific plate recorded by arc volcanism in the South China Sea margin. *Gondwana Res.* 110, 58–72. doi:10.1016/j.gr.2022.05.018

Yan, Q., Shi, X., Liu, J., Wang, K., and Bu, W. (2010). Petrology and geochemistry of Mesozoic granitic rocks from the Nansha micro-block, the South China Sea: constraints on the basement nature. *J. Asian Earth Sci.* 37, 130–139. doi:10.1016/j.jseaes.2009.08.001

Yang, Y., Zhang, H.-F., Chu, Z.-Y., Xie, L., and Wu, F.-Y. (2010). Combined chemical separation of Lu, Hf, Rb, Sr, Sm and Nd from a single rock digest and precise and accurate isotope determinations of Lu–Hf, Rb–Sr and Sm–Nd isotope systems using Multi-Collector ICP-MS and TIMS. *Int. J. Mass Spectrom.* 290, 120–126. doi:10.1016/j.ijms.2009.12.011

Yang, J., Cawood, P. A., Du, Y., Huang, H., Huang, H., and Tao, P. (2012a). Large Igneous Province and magmatic arc sourced Permian–Triassic volcanogenic sediments in China. *Sediment. Geol.* 261-262, 120–131. doi:10.1016/j.sedgeo.2012.03.018

Yang, J. H., Sun, J. F., Zhang, J. H., and Wilde, S. a.J. L. (2012b). Petrogenesis of Late Triassic intrusive rocks in the northern Liaodong Peninsula related to decratonization of the North China Craton: zircon U–Pb age and Hf–O isotope evidence. *Lithos* 153, 108–128. doi:10.1016/j.lithos.2012.06.023

Yang, J.-H., Zhang, J.-H., Chen, J.-Y., and Sun, J.-F. (2020). Mesozoic continental crustal rejuvenation of South China: insights from zircon HfO isotopes of early Jurassic gabbros, syenites and A-type granites. *Lithos* 402-403, 105678. doi:10.1016/j.lithos.2020.105678

Yoder, H. S., Jr., and Tilley, C. E. (1962). Origin of basalt magmas: an Experimental study of natural and synthetic rock systems. *J. Petrology* 3, 342–532. doi:10.1093/petrology/3.3.342

Yu, J.-H., O'reilly, S. Y., Zhou, M.-F., Griffin, W. L., and Wang, L. (2012). U–Pb geochronology and Hf–Nd isotopic geochemistry of the Badu complex, southeastern China: implications for the Precambrian crustal evolution and paleogeography of the Cathaysia block. *Precambrian Res.* 222-223, 424–449. doi:10.1016/j.precamres.2011.07.014

Zhang, F.-Q., Wu, H.-X., Dilek, Y., Zhang, W., Zhu, K.-Y., and Chen, H.-L. (2019). Guadalupian (Permian) onset of subduction zone volcanism and geodynamic turnover from passive-to active-margin tectonics in southeast China. *GSA Bull.* 132, 130–148. doi:10.1130/b32014.1

Zhang, J., Liao, M., Santosh, M., Yang, Z., Zhang, Y., and Dai, Y. (2020). Middle Tonian calc-alkaline picrites, basalts, and basaltic andesites from the Jiangnan Orogen: evidence for rear-arc magmatism. *Precambrian Res.* 350, 105943. doi:10.1016/j.precamres.2020.105943

Zhao, X., and Coe, R. S. (1987). Palaeomagnetic constraints on the collision and rotation of North and South China. *Nature* 327, 141–144. doi:10.1038/327141a0

Zhao, L., Zhou, X., Zhai, M., Santosh, M., and Geng, Y. (2015). Zircon U–Th–Pb–Hf isotopes of the basement rocks in northeastern Cathaysia block, South China: implications for Phanerozoic multiple metamorphic reworking of a Paleoproterozoic terrane. *Gondwana Res.* 28, 246–261. doi:10.1016/j.gr.2014.03.019

Zheng, Y., Chen, Y., Dai, L., and Zhao, Z. (2015). Developing plate tectonics theory from oceanic subduction zones to collisional orogens. *Sci. China Earth Sci.* 58, 1045–1069. doi:10.1007/s11430-015-5097-3

Zhou, X. M., and Li, W. X. (2000). Origin of Late Mesozoic igneous rocks in Southeastern China: implications for lithosphere subduction and underplating of mafic magmas. *Tectonophysics* 326, 269–287. doi:10.1016/s0040-1951(00)00120-7

Zhu, W., Xie, X., Wang, Z., Zhang, D., Zhang, C., Cao, L., et al. (2017). New insights on the origin of the basement of the Xisha uplift, south China sea. *Sci. China Earth Sci.* 60, 2214–2222. doi:10.1007/s11430-017-9089-9